MAIN-SHOCK CHARACTERISTICS

STRONG-MOTION AND BROADBAND TELESEISMIC ANALYSIS OF THE EARTHQUAKE FOR RUPTURE PROCESS AND HAZARDS ASSESSMENT[1]

By David J. Wald and Thomas H. Heaton,
U.S. Geological Survey
and
Donald V. Helmberger,
California Institute of Technology

CONTENTS

ABSTRACT

We have used broadband records from 18 teleseismic stations and three-component records from 16 local strong-motion stations in a formal inversion to determine the temporal and spatial distribution of slip during the earthquake. Separate inversions of the teleseismic (periods, 3–30 s) and strong-motion (periods, 1–5 s) data sets result in similar source models. The data require bilateral rupture, with relatively little slip in the region directly updip from the hypocenter. Slip is concentrated in two patches: one centered 6 km northwest of the hypocenter at 12-km depth with an average slip amplitude of 250 cm, and the other centered about 5 km southeast of the hypocenter at 16-km depth with an average slip amplitude of 180 cm. This bilateral rupture results in large-amplitude ground motions at sites both to the northwest and southeast along the fault strike. The northwestern patch, however, has a larger seismic moment and overall stress drop and thus is the source of the highest ground-motion velocities, a result consistent with observations. The bilateral rupture also results in relatively moderate ground motion directly updip from the hypocenter, in agreement with the ground motions observed at Corralitos, Calif. Furthermore, there is clear evidence of a foreshock (M~4.5–5.0) or slow rupture nucleation about 2 s before the main rupture; the origin time implied by strong-motion trigger times is systematically nearly 2 s later than that predicted from the high-gain regional-network data. The seismic moment obtained from either or both data sets is about 3.0×10^{26} dyne-cm, and the seismic potency is 0.95 km^3. Our analysis indicates that the rupture model determined from the teleseismic data set alone, independent of the strong-motion data set, is adequate to predict many characteristics of the local-strong-motion recordings.

INTRODUCTION

In this study, we use a least-squares linear inversion of strong-motion and teleseismic data to solve for the spatial and temporal distribution of slip during the 1989 Loma Prieta earthquake (M_S=7.1). Although the geometry of the fault plane is fixed in the inversion, we chose it to be compatible with the teleseismic waveforms and the aftershock distribution. Our estimates of the spatial and tem-

[1] Contribution No. 4935, Division of Geological and Planetary Sciences, California Institute of Technology, Pasadena, CA 91125.

poral distribution of slip should enhance studies of fault segmentation and earthquake recurrence (Working Group on California Earthquake Probabilities, 1988; King and others, 1990), which depend on reliable estimates of the rupture dimensions and slip amplitude. Furthermore, the variation in rake angle as a function of position along strike and downdip on the fault plane is critical to analyses of the complex fault interactions within the Sargent-San Andreas fault system (Dietz and Ellsworth, 1990; Olson, 1990; Schwartz and others, 1990; Seeber and Armbruster, 1990).

We use the method of Hartzell and Heaton (1983), which has been shown to provide valuable insight into the rupture history of other California earthquakes (Hartzell and Heaton, 1986; Mendoza and Hartzell, 1988; Wald and others, 1990), as have other finite-fault approaches (Olson and Apsel, 1982; Archuleta, 1984; Beroza and Spudich, 1988). In addition to providing an estimate of the rupture history for individual earthquakes, these studies also give new insight into the general characteristics of the rupture process that are common to many events. After studying slip models for several earthquakes, Mendoza and Hartzell (1988) suggested that large gaps in aftershock patterns commonly coincide with regions of relatively high slip. From the distribution of slip, we can also constrain the location and depth extent of significant energy release and characterize the distribution of stress changes on the fault. These results provide a starting point for calculating ground motions in future events comparable in size to the 1989 Loma Prieta earthquake. Such ground-motion calculations are important for augmenting the sparse data base of near-source strong-motion recordings of $M \geq 7$ crustal earthquakes.

The 1989 Loma Prieta earthquake was well recorded at both local-strong-motion and teleseismic broadband stations. The strong-motion velocity recordings used here are dominated by energy in the range 1–5 s, whereas the broadband teleseismic recordings show energy in the range 3–30 s. This wealth of data provides an opportunity to compare rupture models that are derived independently from either strong-motion or teleseismic data sets with those derived from combined data sets and over a wide range of frequencies. Our results give insight into the limitations of previous studies that used less extensive data sets.

DATA

Ground motions from the 1989 Loma Prieta earthquake were recorded over a wide range of frequencies and distances, from high-frequency waveforms observed on local accelerometers and regional seismic networks to very low frequency waveforms observed in teleseismic surface waves and geodetic line-length changes. Deterministic waveform inversion of high-frequency (>3 Hz) motion, however, requires an accurate and detailed knowledge of the wave propagation in the geologically complex structure of the Loma Prieta region. Furthermore, inversion of high-frequency waveforms requires a proliferation of free variables that significantly increases computation time and decreases the stability of the inversion process. Therefore, we chose to concentrate our study on the lower-frequency part of the rupture history. Near-source, low-pass-filtered strong-motion and teleseismic body waves seem to be the most suitable data sets to study the general characteristics of the slip history. Although geodetic data can also provide important constraints on an earthquake slip-distribution model, they can be overly sensitive to the geometry of the inferred fault plane and so are not always suitable for determining detailed variations in slip.

TELESEISMIC WAVEFORMS

The teleseismic stations chosen for this study are listed in table 1. The data are digital recordings obtained from Chinese Digital Seismograph Network (CDSN), Institut National des Sciences de l'Univers, France (GEOSCOPE), and Incorporated Research Institution for Seismology (IRIS) broadband components and Global Digital Seismograph Network (GDSN) intermediate-period components. These stations provide a uniform azimuthal coverage of the focal sphere and contain several near-nodal observations for both *P*- and *SH*-wave source radiation (fig. 1). In this analysis, instrument responses were deconvolved from the original recordings to obtain true ground velocities.

STRONG MOTION

The distribution of near-source ground velocities used in this study is mapped in figure 2; station abbreviations, station geometries with respect to the epicenter, and trigger times (where available) are listed in table 2. The velocity waveforms were obtained by integrating corrected acceleration recordings provided by the California Division of Mines and Geology (CDMG) (Shakal and others, 1989) and the U.S. Geological Survey (USGS) (Maley and others, 1989), and uncorrected recordings from the University of California, Santa Cruz (UCSC). The velocity waveforms were bandpass filtered between 0.1 and 1.0 Hz, using a zero-phase, third-order Butterworth filter. The horizontal components are rotated with respect to the epicenter to obtain "radial" and "tangential" components. Although this rotation is correct for energy originating near the epicenter, it is only approximate for source regions farther northwest and southeast along the fault.

Table 1.—*Teleseismic stations used in this study*

Station (fig. 1)	Distance (°)	Azimuth (°)	Backazimuth (°)	Phases used
AFI	69.2	232.6	040.8	*P, SH*
ARU	86.9	359.7	000.4	*P, SH*
CAY	70.8	098.6	307.6	*P, SH*
COL	31.8	339.4	138.5	*P*
HIA	77.9	324.0	045.9	*P*
HON	35.0	253.5	055.2	*P*
HRV	38.5	065.7	279.2	*P*
MDJ	76.0	305.2	051.3	*P*
NNA	64.8	130.1	321.5	*P, SH*
OBN	85.1	011.9	343.0	*P, SH*
PPT	60.5	210.6	025.2	*P, SH*
RPN	65.2	167.7	349.0	*P, SH*
SCP	34.1	067.8	278.3	*P*
SSB	84.6	034.7	319.8	*P*
TOL	84.3	043.0	314.8	*P, SH*
WFM	38.5	065.6	279.1	*P*

Two criteria were used to select stations for inclusion in the inversion: The observations should be both close to the aftershock zone and well distributed in azimuth. Within the epicentral region, peak ground motions are relatively independent of surface geology (Benuska, 1990). Care was also taken to avoid stations that seemed to have unusual site responses. For this reason, the CDMG station Agnew was not used, although it is at a similar distance and azimuth to station LEX (fig. 2). UCSC stations BRN, LGP, UCS, and WAH were included to provide important station coverage to the west and southwest of the epicenter. These stations, however, did not record absolute time and required additional processing to remove a few random spikes in the raw acceleration data. Although the despiking process that we used may be inadequate at high frequencies, it provides useful velocity recordings at the frequencies of interest in this analysis (0.1–1 Hz). The station LGP acceleration recording exhibited a permanent step on the vertical component that does not carry through in our bandpassed data; the horizontal components were apparently unaffected. Station BRN was set for 0.5 *g* maximum amplitude, and because amplitude reached close to that value, the accuracy of the response is unknown. We address the issue of estimating absolute time for these stations in the section below entitled "Inversion Method."

FAULT-RUPTURE MODEL

The fault parametrization and modeling procedure that we employ was described by Hartzell and Heaton (1983) in their study of the 1979 Imperial Valley, Calif., earthquake. Faulting is represented as slip on a planar surface that is discretized into numerous subfaults. The ground motion at a given station can be represented as a linear sum of subfault contributions, each appropriately delayed in time to simulate fault rupture. Formal inversion procedures are then used to deduce the slip distribution on these subfaults that minimizes the difference between the observed and synthetic waveforms.

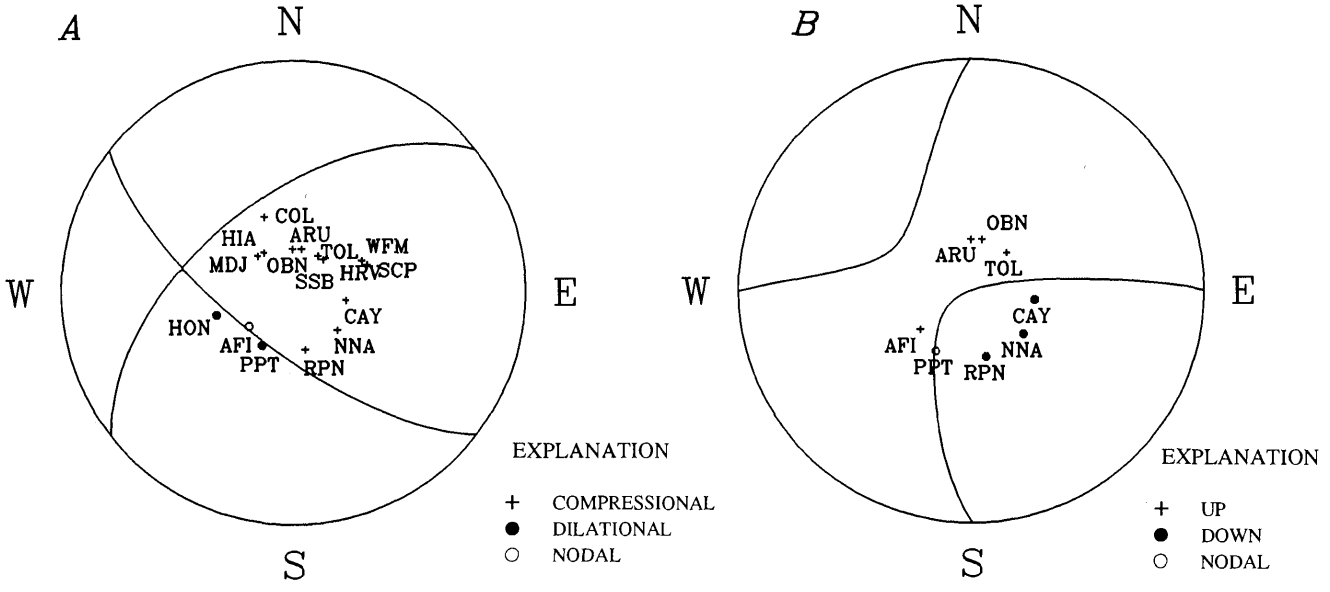

Figure 1.—Focal spheres with plot of takeoff angles of *P* (*A*) and *SH* (*B*) waves from 1989 Loma Prieta earthquake, showing global distribution of broadband teleseismic stations used in this study. Radiation patterns are for a source mechanism with a strike of 128°, a dip of 70°, and a rake of 138°. For *SH* waves, "up" refers to clockwise motion.

In this study, we represent the Loma Prieta rupture as a 40-km-long plane striking N. 128° E. and dipping 70° SW. As a point of reference, the northernmost corner of our assumed fault plane in at lat 37.193° N., long 122.020° W. The fault extends from 1.5- to 20.3-km depth and has a downdip width of 20 km (fig. 3).

We chose the overall dimensions of the fault to enclose the region of major aftershock activity (Dietz and Ellsworth, 1990); possible vertical strike-slip faulting on a second plane extending past the south end of our inferred rupture area is discussed below. The strike and dip of our fault plane (128° and 70°, respectively) were chosen from the broadband-inversion results of Kanamori and Satake (1990). This fault plane is also consistent with the aftershock lineation (Dietz and Ellsworth, 1990), the focal mechanism determined from first-motion data (Oppenheimer, 1990) and the *P*- and *SH*-wave teleseismic waveforms plotted in figure 4. Slight discrepancies in strike and dip would have little effect on our model results and conclusions.

The fault-plane geometry chosen for this study differs somewhat from that used by Lisowski and others (1990) to model the geodetic data. Although they also used a dip of 70°, they found that a strike of N. 136° E. (8° more northerly than ours) was needed to explain their data. Furthermore, their fault plane was shifted about 2 km to the west of our assumed plane, which was chosen to coincide with the aftershock distribution. In general, the geodetic data are more sensitive to fault geometry than are the waveform data, but they are not as powerful in resolving details of the slip distribution. Differences in the fault geometry inferred from static offsets, in comparison with waveform studies, may reflect complexities in the rupture process, such as a nonplanar fault surface or multiple-fault rupture. These complexities are not considered further in this study.

Our fault plane is discretized into 12 subfaults along strike and 8 subfaults downdip, each 2.5 km long and 3.33 km wide vertically (fig. 3). This subfault area is a compromise chosen to give sufficient freedom so as to allow the rupture variations needed to successfully model the ground motions and yet minimize computation time. The computation time for the inversion is proportional to the cube of the number of unknown parameters, in this

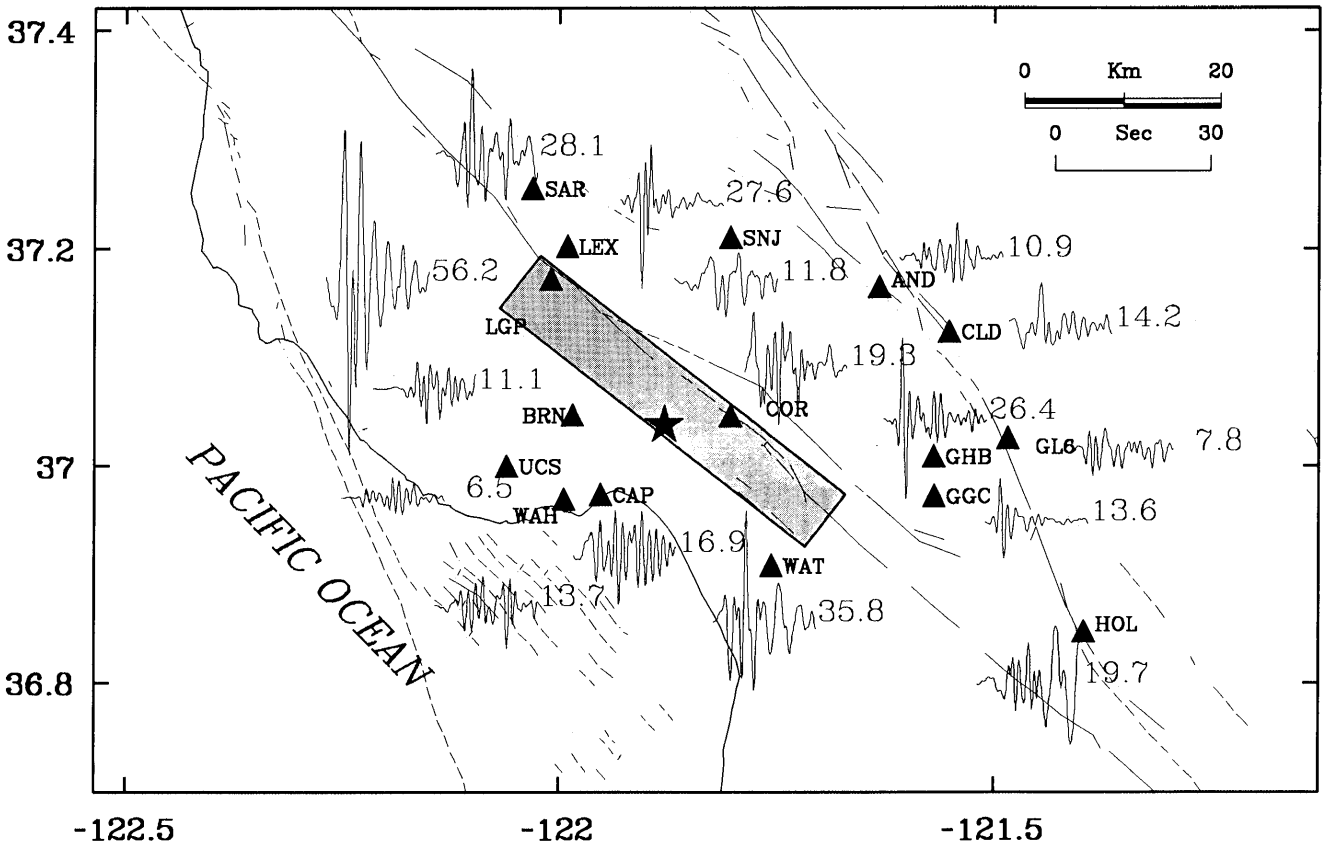

Figure 2.—Loma Prieta region, Calif., showing locations of strong-motion stations (triangles), epicenter of 1989 earthquake (star), and surface projection of model fault plane used in this study (shaded rectangle). Curves represent seismograms of radial (*A*) and tangential (*B*) components of velocity recorded at each station; number to right of each curve is peak velocity (in centimeters per second). Irregular thin lines, faults (dashed where inferred), digitized from major Quaternary faults mapped by Jennings (1975). Crosses (fig. 2*B*), aftershocks. Dashed outline (fig. 2*C*), modified Mercalli intensity (MMI) contour separating regions of MMI VII and VIII (from Stover and others, 1990).

case, the number of subfault slip amplitudes to be determined.

SYNTHETIC GREEN'S FUNCTIONS

The synthetic ground-motion contribution for each subfault was computed by using the Green's function summation and interpolation method of Heaton (1982) briefly summarized here. The subfault motions were obtained by summing the responses of numerous point sources distributed over each subfault. A total of 25 equally spaced point sources (see fig. 3), appropriately lagged in time, were summed to include the traveltime difference due to the varying source positions and to simulate the propagation of the rupture front across each subfault. In all, 2,400 point sources were summed to construct the teleseismic and strong-motion synthetic seismograms at each station for both a pure strike-slip and a pure dip-slip mechanism. Thus, each subfault includes the effects of directivity.

The point-source responses, or Green's functions, for teleseismic *P*- or *SH* body-wave synthetic seismograms were computed by using the generalized ray method (Langston and Helmberger, 1975). We included the responses of all rays up to two internal reflections in a layered velocity model, including free-surface and internal-phase conversions. A Q operator (Futterman, 1962) was applied, with an attenuation-time constant t^* of 1 and 4 s for *P* and *SH* waves, respectively.

The point-source responses for the strong motions were computed for a layered velocity model, using the discrete-wavenumber/finite-element (DWFE) methodology of Olson and others (1984) for frequencies as high as 3.5 Hz. In practice, we calculated a master set of synthetic seismograms for increments in depth from 1.5 to 20.3 km and for ranges of 0 to 75 km, to allow for the closest and farthest possible subfault-station combinations. Then, for each subfault-station pair, the required subfault response was derived by the summation of 25 point-source responses obtained by linear interpolation of the closest Green's functions available in the master set. The linear interpolation of adjacent Green's functions was performed by aligning the waveforms according to their shear-wave traveltimes. Subfault contributions from both a pure dip-slip and pure right-lateral strike-slip mechanism were then computed, using the assumed fault geometry. The relative weights of these fundamental mechanisms, as well as the amount of slip on each subfault, were determined in the inversion process, as described below.

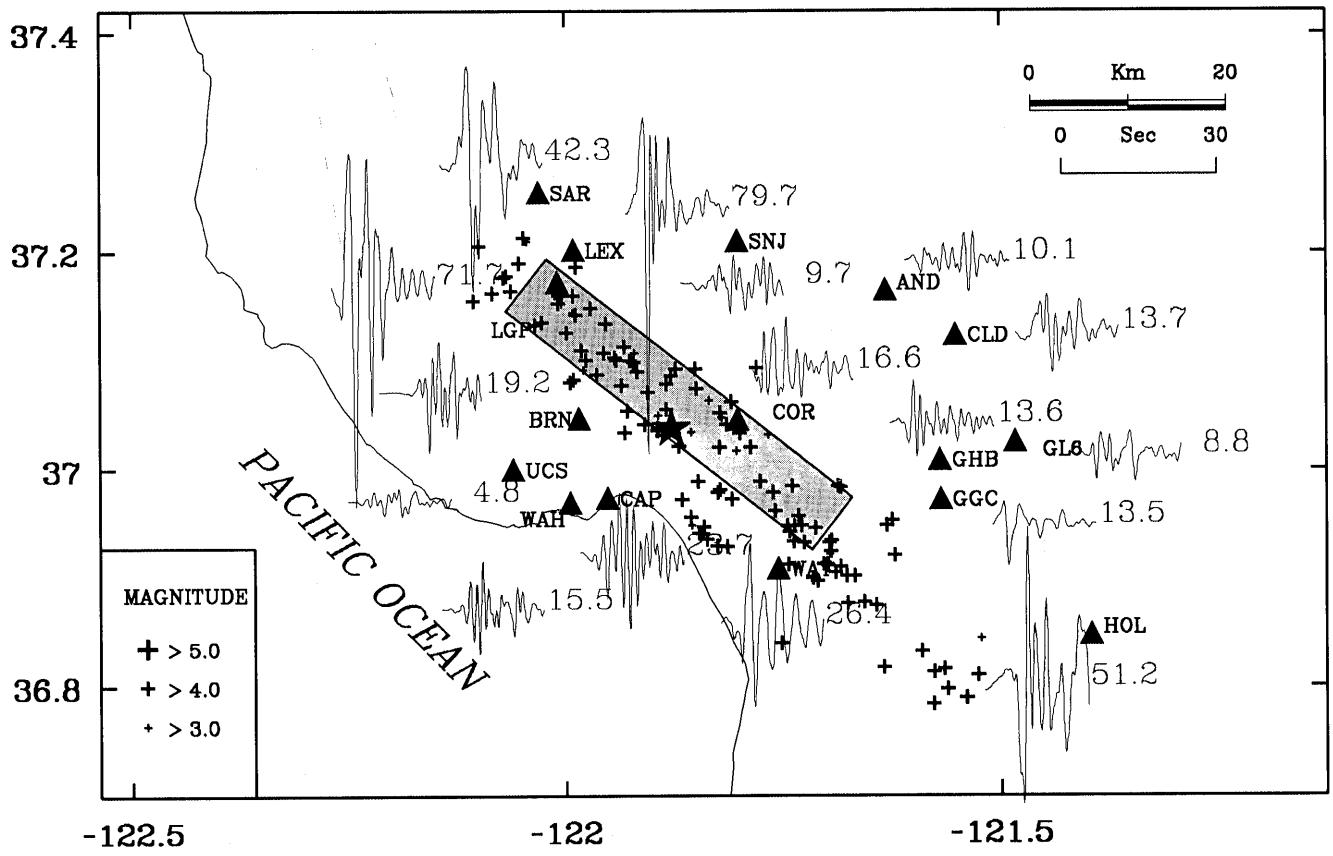

Figure 2.—Continued

Table 2.—*Strong-motion stations in the Loma Prieta region*

[Data sources: CDMG, California Division of Mines and Geology; UCSC, University of California, Santa Cruz; USGS, U.S. Geological Survey. Distance and azimuth measured from epicenter at lat 37°02.37′ N., long 121°52.81′ W. Station display adjusted to absolute time (see text). Trigger times measured from 0004:00.00 G.m.t. October 18, 1989; origin time measured from main shock at 0004:15.21 G.m.t. October 18, 1989]

Station (fig. 2)	Station name	Data source	Station No.	Distance (km)	Azimuth (°)	Delay (s)	Trigger time (s)	Origin time (s)
AND	Anderson Dam, downstream	USGS	1652	26.1	057.6	0.0	23.0	7.8
BRN	Branciforte Drive	UCSC	---	9.5	275.4	--	--	--
CAP	Capitola Fire Station	CDMG	47125	9.7	222.0	--	--	--
CLD	Coyote Lake Dam	CDMG	57504	30.7	072.1	.0	24.5	9.3
COR	Corralitos	CDMG	57007	6.8	083.5	.0	20.4	5.2
GGC	Gavilan College	CDMG	47006	28.6	104.8	–.4	[1]23.9	8.7
GHB	Gilroy Historical Building	CDMG	57476	27.8	096.9	–.2	23.4	8.2
GL6	Gilroy array station 6	CDMG	57383	35.2	092.4	.7	26.0	10.8
HOL	Hollister, Pine Street	CDMG	47391	47.9	116.3	1.9	27.5	12.3
LEX	Lexington Dam	CDMG	57180	19.1	331.0	–.3	21.1	5.9
LGP	Los Gatos Presentation Center	UCSC	---	18.8	321.7	--	--	--
SAR	Saratoga, Aloha Avenue	CDMG	58065	27.5	330.6	--	--	--
SNJ	San Jose, Santa Theresa	CDMG	57563	20.1	019.6	–.2	18.3	[2]3.1
UCS	University of California, Santa Cruz	UCSC	---	16.8	255.0	--	--	--
WAH	Walter's house	UCSC	---	12.9	233.4	--	--	--
WAT	Watsonville	CDMG	47459	18.1	142.8	.3	21.6	6.4

[1]Accurately estimated from time at Gilroy array station 1.
[2]Digital instrument with memory before trigger time (*P* wave at 1.7 s).

VELOCITY MODEL

The velocity model used to compute the DWFE Green's functions is listed in table 3. *P*-wave velocities were calculated by averaging the two velocity-depth profiles constructed by Dietz and Ellsworth (1990) for regions northeast and southwest of the San Andreas fault. We added a thin, lower-velocity layer to this model to better approximate elastic properties just beneath the strong-motion stations. *S*-wave velocities were calculated by assuming that the structure is a Poisson solid.

The velocity model used to compute the teleseismic Green's functions (table 4) is a four-layer approximation to the local-velocity structure used in the strong-motion

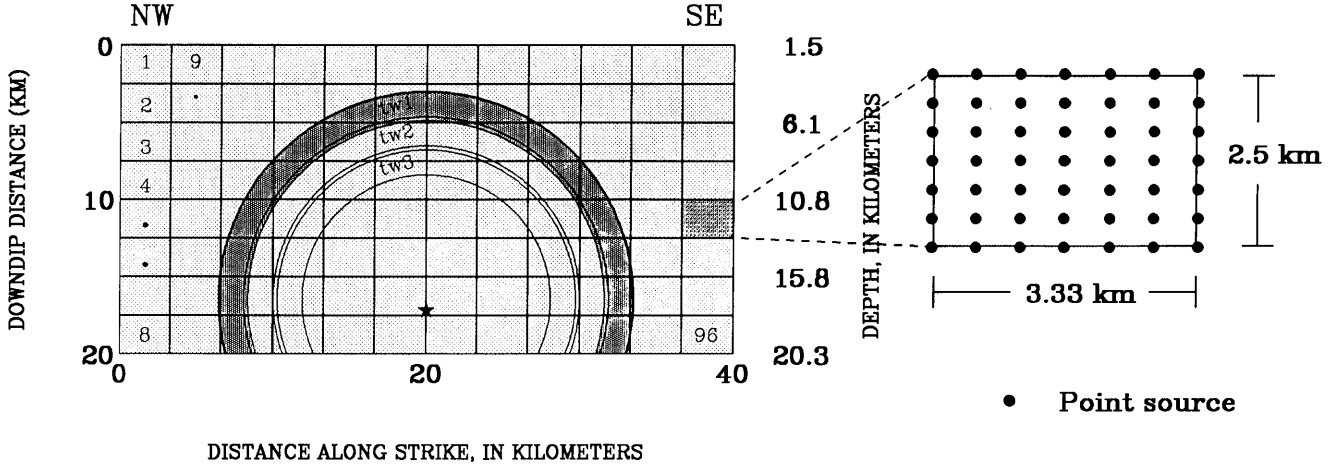

Figure 3.—Northwest-southeast cross section of fault-rupture model along fault plane, showing layout of subfaults (numbers 1–96) used in analysis. Enlargement shows distribution of point sources within each subfault. Largest circle radiating outward from hypocenter (star) represents position of rupture front after 5 s; smaller concentric circles delimit (slightly overlapping) fault regions slipping in time windows 1 (tw1, shaded), 2 (tw2), and 3 (tw3) (see fig. 18).

inversion (table 3). Heaton and Heaton (1989) discussed difficulties that arise when the seismic moments derived from different velocity models are compared. In this example, the seismic velocities are nearly constant for both the teleseismic and strong-motion velocity models in the depth range 7–18 km (the region of highest slip). This

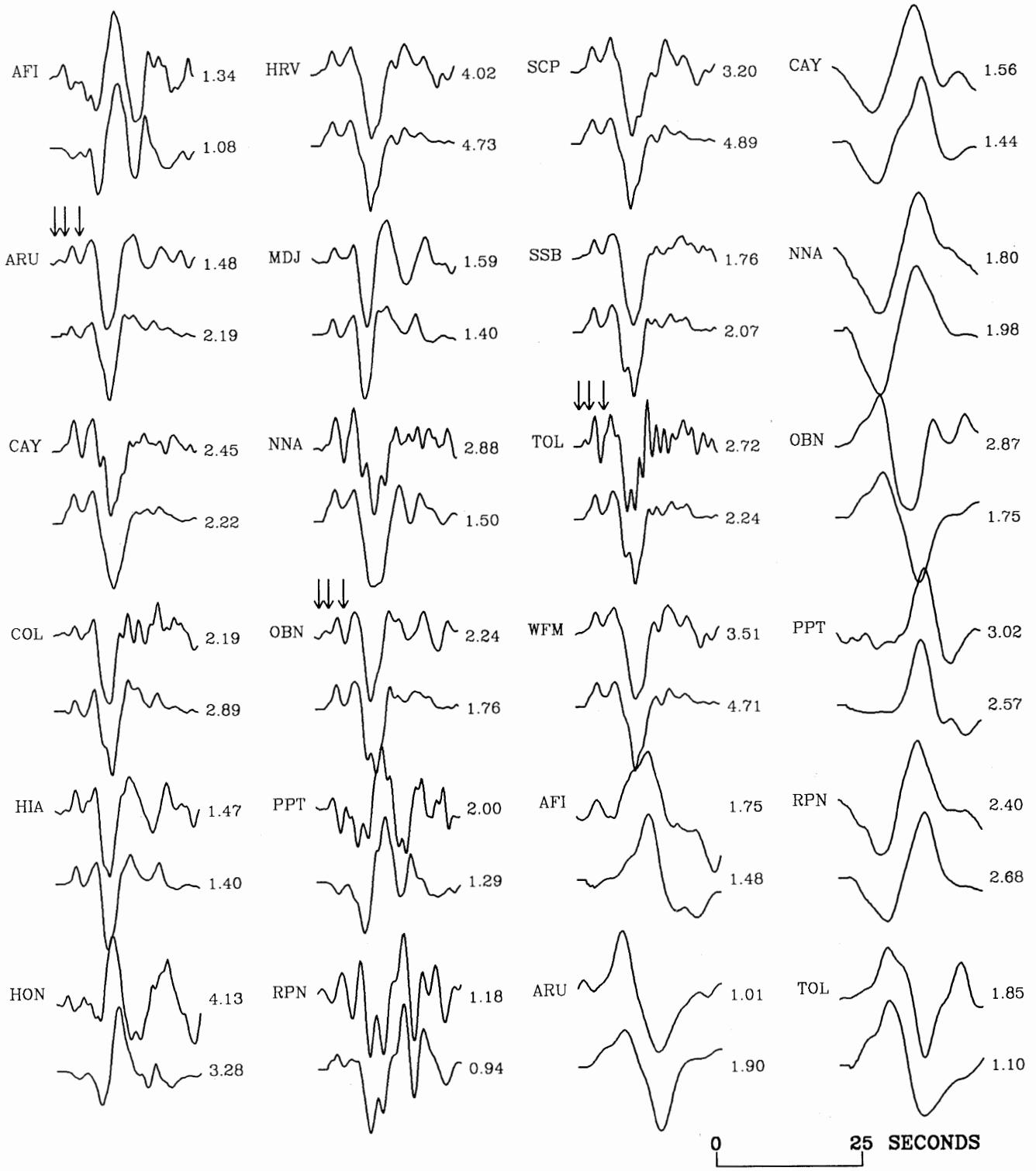

Figure 4.—Comparison of observed (upper curve) and synthetic (lower curve) seismograms recorded at broadband teleseismic stations (see fig. 1 for locations). First 16 stations are *P* waves, and last 8 stations are *SH* waves. Arrows denote arrivals detailed in figure 8.

Table 3.—*Loma Prieta velocity structure for strong-motion data modeling*

[V_p, *P*-wave velocity; V_s, *S*-wave velocity]

V_p (km/s)	V_s (km/s)	Density (g/cm^3)	Thickness (km)	Depth (km)
1.73	1.00	1.50	0.1	0.1
3.38	1.95	1.55	.4	.5
4.29	2.48	1.85	.5	1.0
4.80	2.77	2.05	2.0	3.0
5.37	3.10	2.26	2.0	5.0
5.74	3.31	2.45	2.0	7.0
6.15	3.55	2.58	2.0	9.0
6.25	3.61	2.62	4.0	13.0
6.27	3.62	2.63	5.0	18.0
6.67	3.85	2.77	7.0	25.0
8.00	4.62	3.28	50.0	---

Table 4.—*Loma Prieta velocity structure for teleseismic data modeling*

[V_p, *P*-wave velocity; V_s, *S*-wave velocity]

V_p (km/s)	V_s (km/s)	Density (g/cm^3)	Thickness (km)	Depth (km)
4.60	2.66	2.60	3.5	3.5
6.05	3.49	2.65	6.5	10.0
6.30	3.64	2.67	14.0	24.0
8.00	4.62	3.28	---	---

favorable coincidence means that a simple comparison of the seismic moments derived from teleseismic and strong-motion inversions is approximately valid.

SOURCE-TIME FUNCTION AND RUPTURE VELOCITY

The subfault synthetic seismograms are convolved with a dislocation-time history that we represent by the integral of an isosceles triangle with a duration of 0.7 s. This slip function was chosen on the basis of comparison of the synthetic velocity-pulse width for a single subfault with the shortest velocity-pulse width observed, as well as from previous experience with this inversion method (Heaton, 1990). As Hartzell and Mendoza (1991) pointed out, resolution of the slip function is difficult, although we are required by the strong-motion recordings to use a relatively short (<0.8 s) duration.

The rupture velocity is assumed to be a constant 2.7 km/s, or 75 percent of the shear-wave velocity in the main source region (table 3). Many observations, including the absence of tectonic surface slip (U.S. Geological Survey staff, 1990), indicate that little dislocation occurred above 4-km depth. The position of the rupture front 5 s after the nucleation time is mapped in figure 3.

Some flexibility in the rupture-velocity and slip-time history is achieved by introducing time windows (Hartzell and Heaton, 1983). In all inversions, each subfault is allowed to slip in any of three identical 0.7-s time windows after passage of the rupture front, thereby allowing for a possibly longer slip duration or a locally lower rupture velocity. Hartzell and Mendoza (1991) obtained nearly identical dislocation models for the 1978 Tabas, Iran, earthquake (M_S=7.4) using both a linear inversion parametrizing slip with three time windows (as is done here) and a nonlinear iterative inversion that allows a single rupture at each point on the fault but a varying rupture velocity.

In this study, each time window is separated by 0.6 s, allowing a small overlap in the 0.7-s-duration subfault source-time function. Thus, as mapped in figure 3, the region of the fault that is allowed to slip 5 s (for example) after rupture nucleation is within concentric bands occupied by the three time windows. We did not test for the possibility of a faster rupture velocity because initial indications from our modeling showed that regions toward the northwest required slightly lower rupture velocities than 2.7 km/s, which can be approximated given the flexibility allowed for by the three time windows.

INVERSION METHOD

A constrained, damped, linear least-squares inversion was used to determine the subfault dislocations that give the best fit to the strong-motion velocity waveforms. The inversion is stabilized by requiring that the slip be everywhere positive and that the difference in dislocation between adjacent subfaults (during each time window), as well as the total seismic moment, be minimized, as discussed by Hartzell and Heaton (1983).

Smoothing, or minimizing the difference is slip between adjacent subfaults, is required to avoid instabilities, as well as downplay the role in the inversion played by starting and stopping phases associated with each subfault. If large variations in slip are allowed, such phases dominate, although they represent artifacts of the subfault discretization. Because numerous subfaults are required to resolve the spatial variations in slip, smoothing constraints are needed. We expect the smoothing required for the teleseismic and strong-motion data to differ, in that the number of subfaults and their size remain fixed for each data set, although the dominant period of the energy varies.

The teleseismic data can generally be fitted with somewhat-isolated spikes of large slip, which would predict enormous (unphysical) localized slips and excessive high-frequency radiation. Thus, in practice, we increase the spatial-slip smoothing until the waveform fits begin to

degrade. Because the strong-motion inversion is more sensitive to higher-frequency radiation, the inversion automatically limits extreme variations in rupture, which produce excessive short-period radiation. Therefore, the strong-motion inversion needs minor additional smoothing. And in fact, substantial smoothing would degrade the strong-motion waveform fits.

In essence then, the teleseismic rupture model may represent a lower bound on the actual fault roughness and thus represents a lower limit to high-frequency radiation. Similarly, we might expect the strong-motion model, derived from velocity waveforms, to underestimate much-higher-frequency accelerations, but it may be adequate for frequencies slightly higher than used in the inversion, possibly as high as 5 Hz.

Both the strong-motion observations and subfault synthetic seismograms were bandpass filtered from 0.1 to 1.0 Hz with a zero-phase Butterworth filter and resampled at a uniform rate of 10 samples per second. The teleseismic data were similarly filtered from 0.02 to 1.0 Hz with a time step of 10 samples per second. The upper-frequency limit is imposed by the characteristics of the strong-motion recordings. In general, more coherence is noticeable in the waveforms at periods above 1 s than at higher frequencies. Originally, the strong-motion data were low-pass filtered at 3 Hz, but we noticed significant complexity, apparently caused by local site responses. We modeled the first 25 s of the record for teleseismic data and between 14 to 22 s of the strong-motion records (depending on the individual record).

TIMING

The initial alignment over time of the observed and synthetic seismograms is a critical issue in modeling waveform data to determine the temporal and spatial distribution of slip on the fault plane. In this type of study, two approaches are possible. One approach (commonly used for teleseismic-waveform inversions) is to time-shift the synthetic waveform from a point-source hypocenter until the first significant motion aligns with that of the observed recording. Later source contributions (from the developing rupture process) can then be determined by modeling the remaining features of the record. This method is adequate when (1) the observed first arrival time is unambiguous and (2) the initial arrival is actually from the locally determined hypocenter (including the origin time). However, the first arrivals (observed on local seismic networks) for waves from the hypocenter may be too small to be seen teleseismically or on strong-motion recordings. These first arrivals are used to determine the hypocenter and origin time of the earthquake. Serious problems arise if the first arrival on a teleseismic-waveform or strong-motion record is erroneously assumed to be from the hypocenter determined from local-seismic-network data. Hartzell and Heaton (1983) showed how serious this problem is when interpreting the 1979 Imperial Valley, Calif., earthquake.

In the second approach, all correlations are done in absolute time, with appropriate time delays to accommodate errors introduced by inadequacies of the assumed velocity model. At teleseismic distances, these delays can be substantial, and so master-event techniques must be used (for example, Hartzell and Heaton, 1983). For local-strong-motion data, the use of absolute time is preferable if it is known for most of the recordings. We use this second approach in our strong-motion-modeling study.

When the trigger time on local strong-motion records is available (see table 2), both the observed and synthetic waveforms are aligned in absolute time. Slight adjustments are also made to allow for variations in traveltime not predicted by the assumed one-dimensional velocity structure (station delays, table 2). Although this procedure provides an approximate, static station delay, it does not eliminate timing errors introduced by lateral variations due to subfault-to-station travelpaths that vary significantly along the fault. This issue can be addressed later with the analysis of aftershock recordings at strong-motion sites when these data are available.

For strong-motion stations without absolute time, both the observed and synthetic waveforms will be aligned is we assume that the initial *P* wave triggers the instrument. The stations with timing are weighted heavily in the inversion, and those without timing are downweighted, effectively removing them from the inversion. Using the preliminary inversion results, synthetic waveforms were calculated for those stations without timing, and new time estimates were obtained by comparing the observed with the synthetic waveforms. At some stations (UCS, WAH, fig. 2), the forward modeling was insufficient to estimate the timing, and so these stations were not given significant weighting in subsequent inversions. We did, however, continue to compute waveforms for these stations for comparison with the observed waveforms and for later analysis.

TELESEISMIC MODELING

PRELIMINARY ANALYSIS

Several broadband teleseismic studies of the 1989 Loma Prieta earthquake have been completed; their overall conclusions were summarized by Wallace and others (1991). As pointed out by Choy and Boatwright (1990), three distinct arrivals are recognizable on most of the broadband teleseismic velocity recordings (arrows, fig. 4). The first arrival is quite small but is visible on the *P*-wave records, about 1 s into the trace, at stations ARU, OBN,

and TOL (fig. 1). The first subevent is at the threshold of resolution for waveform modeling of teleseismic data.

In general, previous teleseismic models describe the earthquake as a simple two-point-source combination representing two later, dominant subevents. The seismic moments determined in these broadband studies range from 2.0×10^{26} to 3.0×10^{26} dyne-cm and show a wide variation in the ratio of the seismic moments for the third subevent relative to the second subevent, depending on the assumptions of the individual researcher. In addition, the estimate of the best point-source depths vary widely for the second and third subevents, or for a single estimate of the centroid location. This variation suggests that the rupture, though over a finite area, was not extensive enough to be easily resolved teleseismically (that is, $\lesssim$35 km), a result consistent with the limited extent of the rupture inferred from the aftershock distribution alone (Dietz and Ellsworth, 1990).

When teleseismic velocity waveforms are integrated into the displacements, arrivals become difficult to distinguish from individual subevents. In particular, the arrival from the second subevent appears as a subtle inflection in the large pulse from the third subevent. Although nearly identical results were obtained by modeling the teleseismic displacement waveforms, we find it easier to compare observed and synthetic velocity waveforms.

INVERSION RESULTS

The spatial distribution of slip obtained from inversion of only the teleseismic-waveform data is plotted in figure 5. We use a large contour interval (50 cm) to emphasize the robust features of our model; the dislocations shown represent the combined slip for the three time windows previously mentioned.

Our teleseismic model has a seismic moment of 2.8×10^{26} dyne-cm. The observed teleseismic records (upper curves) are compared with the synthetic seismograms (lower curves) predicted by the teleseismic dislocation model in figure 4. The main features of this model are (1) a two-lobed bilateral rupture with a slightly higher slip to the northwest, (2) concentration of the highest slip at a depth of 11 km for the northwestern patch and slightly deeper for the southeastern patch, and (3) low slip in the region updip from the hypocenter.

Directivity controls the waveform and amplitude only when the rupture front propagates at a velocity comparable to that of the phase of interest. Thus, the teleseismic body waves, all with steep takeoff angles, are limited in their ability to resolve rupture directivity along strike but are quite sensitive to updip or downdip rupture propagation. The absence of vertical directivity is apparent in our solution. Because the teleseismic-waveform data do not allow significant slip updip or downdip from the hypocenter, most slip must occur along strike from the hypocenter. Bilateral rupture is indicated by the timing of the second and third arrivals and by the absence of significant azimuthal arrival-time differences between the two dominant arrivals. As discussed in the next section, this model explains many of the features observed in the local-strong-motion data.

STRONG-MOTION MODELING

PRELIMINARY ANALYSIS

PEAK MOTIONS

Inspection of the pattern of near-source peak ground velocities (fig. 2) reveals that the largest motions occurred at stations located near the northwest (LEX, LGP, SAR)

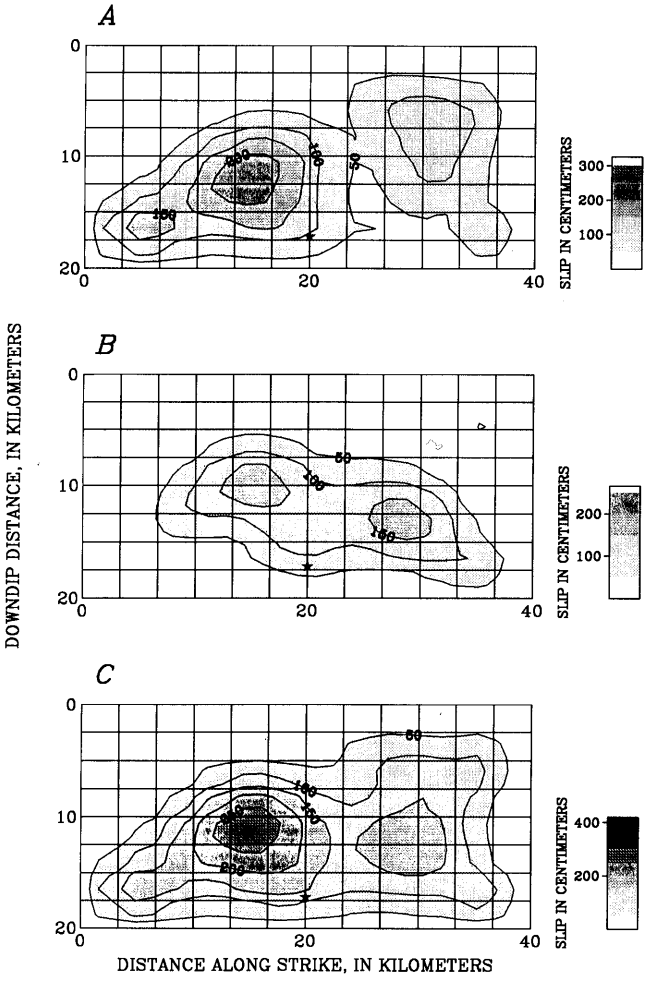

Figure 5.—Northwest-southeast cross section of model fault (fig. 3), showing contours of dislocation for strike slip (*A*), dip slip (*B*), and oblique slip (*C*) predicted from teleseismic inversion. Contour interval, 50 cm. Star, hypocenter of 1989 Loma Prieta earthquake.

and southeast (HOL, WAT, GHB) ends of the aftershock zone. A tendency for large motions at both ends of the aftershock zone, particularly to the northwest, is evident in the modified Mercalli intensity (MMI) VII isoseismal map (fig. 2*C*), in contrast to the relatively small amplitudes recorded at station COR, directly updip from the hypocenter, where we expected to see a strong directivity from a rupture propagating updip.

Additional evidence for bilateral rupture is the timing and similarity of the velocity recordings at stations GGC and SAR (fig. 6); these stations are symmetrically located about the fault plane and at nearly the same epicentral distance (fig. 2). Polarities for the radial and vertical components at station SAR are reversed to correct for the change in sign of the *P*- and *SV*-wave-radiation patterns and to enhance the comparison. Although absolute time unavailable for station SAR, the timing at this station was estimated by noting the similarity of the *S* waveform to that at station LEX (fig. 2) and then correcting for the additional shear-wave-propagation time from station LEX to station SAR. The timing and waveforms of the main arrivals at stations GGC and SAR are similar, although they are slightly earlier at station GGC than at station SAR; however, the peak amplitudes are considerably larger at station SAR (fig. 2). These observations demand a nearly symmetrical, bilateral rupture, with considerably more 1-Hz energy radiated northwestward. A single asperity centered at or above the hypocenter could also explain the symmetry in timing and waveform at these stations, although it is inconsistent with the small amplitudes observed at stations located near the center of the aftershock region (BRN, CAP, COR, UCS, WAH, fig. 2) that should otherwise be enhanced by a slip concentration in the center of the fault. Furthermore, a central asperity cannot easily account for the larger amplitudes observed to the northwest and the lower amplitudes observed to the south-

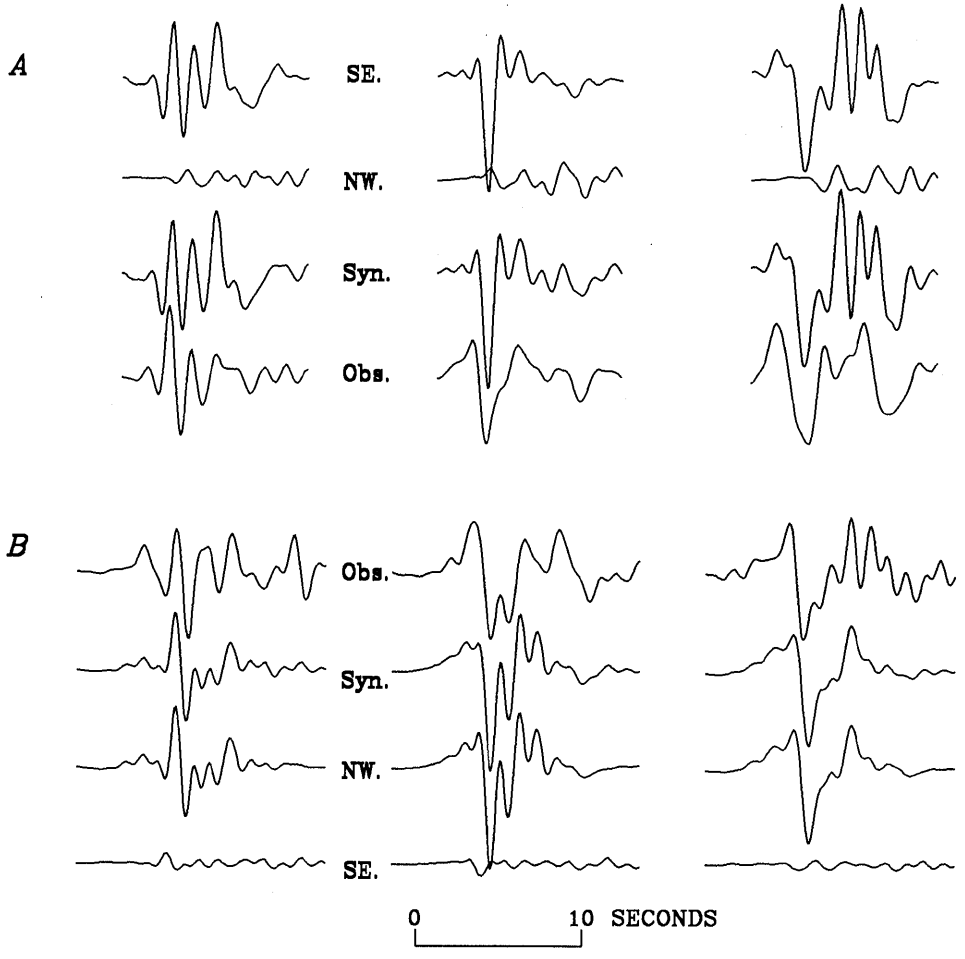

Figure 6.—Comparison of radial (left), tangential (middle), and vertical (right) components of velocity recorded at strong-motion stations GGC (*A*) and SAR (*B*) (see fig. 2 for locations), aligned vertically in absolute time, normalized to peak velocity, and shown at same scale. Polarities of components are reversed in figure 6*B* to enhance comparison. Obs., observed seismograms; syn., synthetic seismograms, with contributions from northwest (NW.) and southeast (SE.) halves of model fault.

east. These observations agree with the main features found from inversion of the teleseismic-waveform data.

TRIGGER TIMES AND RUPTURE INITIATION

We use the hypocentral parameters of Dietz and Ellsworth (1990), as listed in table 2. In figure 7, we compare the theoretical *P*-wave traveltimes at each station with the corresponding trigger times. Because strong-motion accelerometers are triggered only by vertical motions, they probably were triggered by *P*-wave arrivals. The accelerometers, however, were actually triggered nearly 2 s later than the *P*-wave arrival time predicted from the hypocentral parameters of Dietz and Ellsworth (1990). At station COR, nearly directly above the hypocenter (fig. 2), the observed trigger time is about 1.8 s after the *P*-wave-arrival time predicted by using the velocity model listed in table 3. Other stations show similar delays. We examine this delay in figure 8 by plotting the waveforms and timing of data from various instrument types: the low- and high-gain vertical components at USGS station BSR, teleseismic station TOL, strong-motion station SAR, and station SAO (San Andreas Geophysical Observatory), a University of California, Berkeley, broadband Streckeisen instrument. The waveforms for stations BSR and SAO are aligned on their first motions, and stations TOL and SAR are aligned according to our interpretation of the rupture initiation. That is, the simplest explanation for this 2-s delay is that a foreshock, too small ($M \leq 5$) to trigger the strong-motion instruments, occurred about 2 s before the main rupture; this foreshock was used to locate the hypocenter from the high-gain regional-network data. We suggest, however, that the initial 2 s represents the initial stage of rupture, possibly a smooth, slow growth episode (Wald and others, 1991). As plotted in figure 8, the initial stage of rupture clipped the nearby high-gain station BSR but shows a long-period characteristic in the low-gain component. This low-gain component clipped after about 1.6 s, after which (1) the first teleseismic energy becomes visible, (2) the strong-motion stations begin to trigger, and (3) the local broadband stations change from a long-period one-sided waveform and dramatically clip. These observations can be interpreted as a slow rupture nucleation that generated insufficient long-period energy to be seen teleseismically and insufficient high-frequency radiation to trigger the strong-motion instruments.

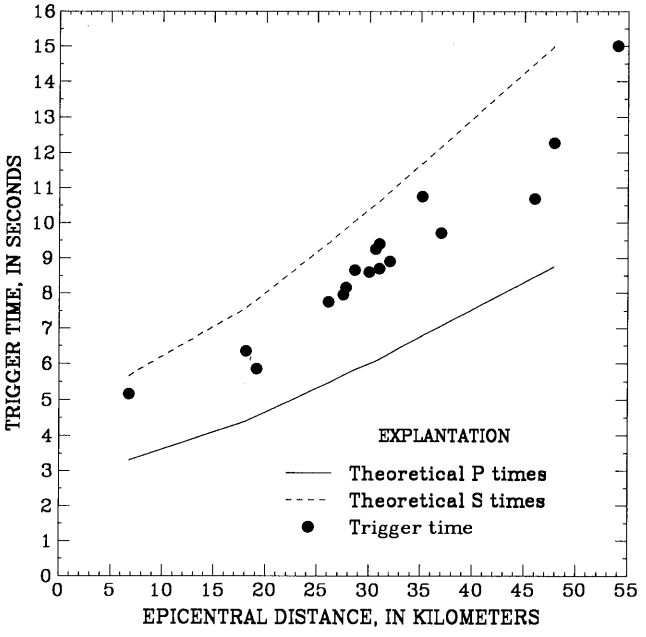

Figure 7.—Strong-motion trigger time versus epicentral distance for velocity model listed in table 3, based on origin time of main shock at 0004:15.21 G.m.t. October 18, 1989. Dot at 7 km distance is COR, Corralitos strong-motion station (fig. 2).

The observation that led to the discovery of this timing problem was the initial inversion of the strong-motion waveforms, using absolute time. The resulting slip-distribution model required a two-lobed pattern similar to that in the teleseismic-waveform data, but the centers of these lobes were forced toward the sides of the fault. This slip distribution was inconsistent with that derived from the teleseismic-waveform data and with the source region suggested by the aftershock pattern (Dietz and Ellsworth, 1990). Furthermore, it generated inferior fits to the strong-motion data.

Thus, the failure to account for this delay can seriously affect source models based on waveform inversion, using absolute timing. In particular, the modeled rupture front would already have progressed 5 km away from the hypocenter during this 2-s interval, when, in fact, probably very little rupture propagation occurred during this period. Owing to the initial weak 1.8 s of rupture, the strong-motion records appear to be delayed by 1.8 s with respect to Dietz and Ellsworth's (1990) origin time. We thus choose to ignore the foreshock or rupture initiation, and we begin modeling at the time of the first significant strong-ground motion. We assume that the main rupture began at or near Dietz and Ellsworth's (1990) hypocentral location 1.8 s after their origin time, and then allow the rupture to propagate outward from that location. This approach is consistent with our analysis of the teleseismic-waveform data, which also begins with the first significant rupture, because the initial rupture or foreshock was too small to be recorded teleseismically.

It is not uncommon for the hypocenter determined from high-gain regional-network data to represent a foreshock or an earlier stage of rupture not observed on other data sets. Wald and others (1990) discussed the rupture process of the 1987 Superstition Hills, Calif., earthquake and suggested that the network hypocenter represents an ear-

lier foreshock and not the main rupture initiation. Therefore, on the basis of the strong-motion and teleseismic data, that event began rupturing in a different location from the hypocentral coordinates determined from the regional-network data.

INVERSION RESULTS

The distribution of slip calculated from the inversion of only the strong-motion velocities is plotted in figure 9, and the observed (upper curve) and synthetic (lower curve) strong-motion velocities are compared in figure 10. The strong-motion rupture model is similar to that derived from the teleseismic inversion (fig. 5). Again, slip is concentrated in two patches, one centered about 8 km northwest of the hypocenter at 12-km depth with a peak slip amplitude of 350 cm, and the other centered about 6 km southeast of the hypocenter at 16-km depth with a peak slip amplitude of 460 cm. These parameters are summarized in table 5. As for the teleseismic inversion, the largest localized slip concentrations are northwest of the hypocenter.

The overall pattern of the strong-motion slip duration and waveform complexity is explainable by the relative positions of individual stations with respect to the two lobes of concentrated slip. The observed (first curve) and synthetic (second curve) velocities at selected strong-motion stations are compared in figure 11, along with the surface projection of the fault plane and strong-motion slip distribution. To better understand our synthetic waveforms, the synthetic seismograms that result from rupture on only the northwest (third curve) and southeast (bottom curve) halves of the fault are also compared in figure 11. A similar breakdown of the synthetic ground motions for all components at stations GGC and SAR (fig. 2) is shown

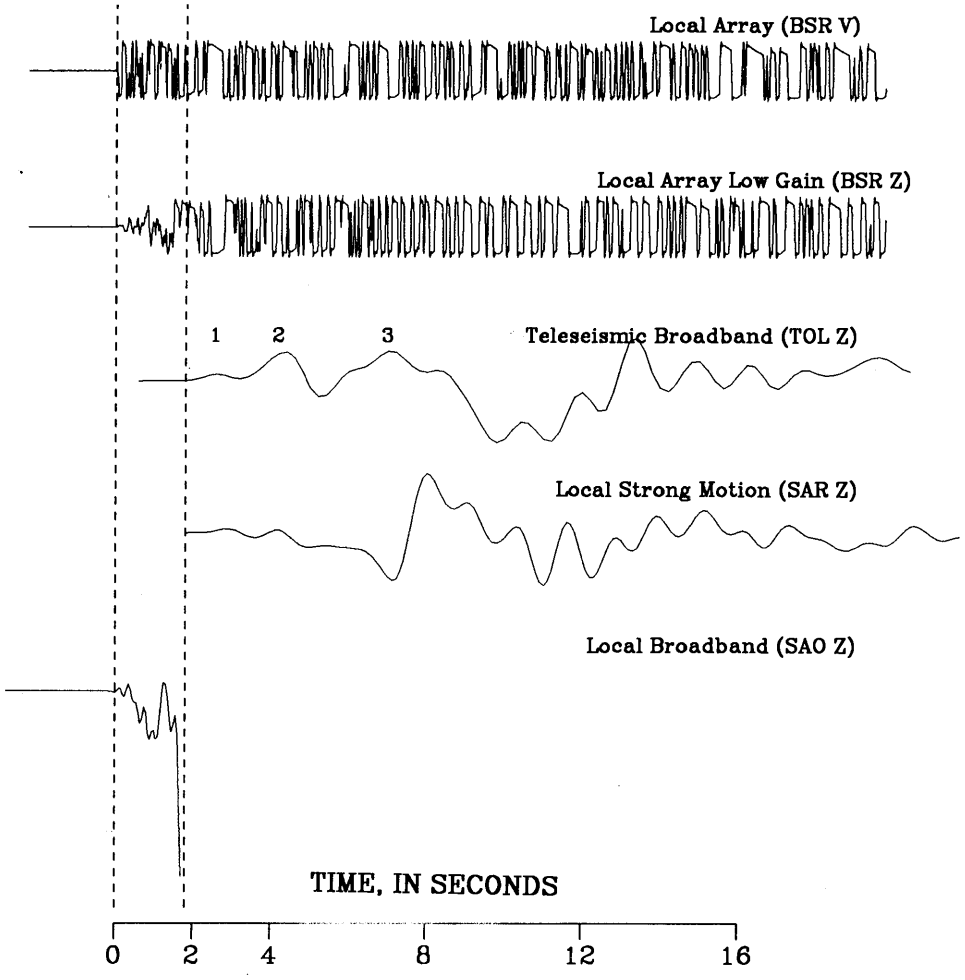

Figure 8.—Comparison of waveforms at broadband teleseismic stations (see fig. 1 for locations) indicating delay to main part of rupture, aligned in absolute time except for record at station TOL. Vertical dashed lines indicate times of 0.0 and 1.8 s. Z, vertical component of velocity. Numbers 1 through 3 on station TOL record refer to arrivals denoted by arrows in figure 4.

in figure 6. Velocities at stations located nearly along strike (LEX, SAR, GGC, GHB, fig. 2) are controlled by the nearby slip concentration and show little contribution from the farther lobe. This result is attributable to both the additional distance from the farther lobe of concentrated slip and the favorable source directivity at stations in the direction of rupture. Thus, the waveforms at alongstrike stations are simple, large in amplitude, and short in duration. Stations in the central section of the fault (CAP, COR, fig. 2) show smaller amplitudes and more waveform complexity, resulting from the absence of rupture directivity and the interference of contributions from the northwest and southeast regions of high slip. We expect these waveforms to be the most difficult to model, because the synthetic seismograms are controlled by interference of the wavefields from two propagating rupture fronts that are diverging from one another.

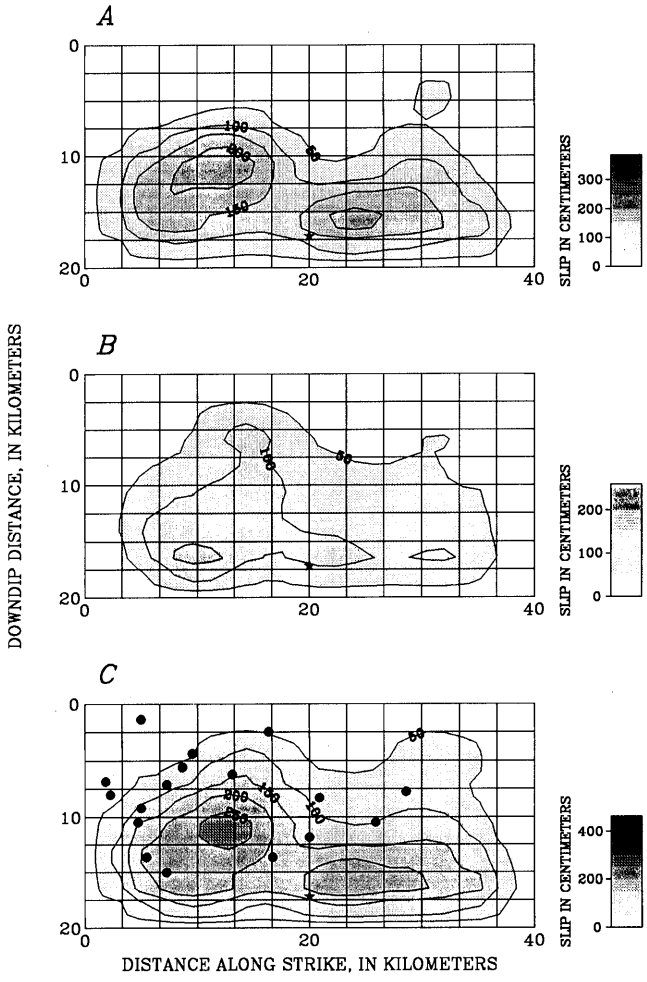

Figure 9.—Northwest-southeast cross section of model fault (fig. 3), showing contours of dislocation for strike slip (*A*), dip slip (*B*), and oblique slip (*C*) predicted from strong-motion inversion. Contour interval, 50 cm. Star, hypocenter of 1989 Loma Prieta earthquake; dots, aftershocks of $M \geq 4.0$ projected onto model fault plane.

SENSITIVITY TO STATION COVERAGE

Of concern when inverting waveform data for source rupture processes is the consideration of possible contamination from site effects and flawed data. John Vidale (oral commun., 1991) suggested that the strong-motion instrument at station LGP (fig. 2) moved during the main shock, resulting in data of questionable reliability. Although we believe that the data from this station are well behaved on the basis of its waveform data, frequency content, and amplitude similarities to the data from neighboring stations LEX and SAR (see figs. 2*B*, 2*C*), we performed a test inversion excluding the data from station LGP to be certain of the role of that station in the final solution. The result indicated that removal of the data from station LGP has almost no effect on the source model. This result might have been anticipated because any single station has only a limited role in the total solution and, in particular, the data from station LGP are nearly redundant, considering that the waveforms at adjacent stations SAR and LEX require a similar source contribution. In fact, forward modeling for station LGP with the solution determined without considering those data fits that record well, confirming our observation that the waveform is properly behaved and dominated by useful source information.

JOINT TELESEISMIC AND STRONG-MOTION INVERSION

Although the teleseismic and strong-motion models have several features in common, variations in the results are apparent. The teleseismic model shows considerably more strike slip in the shallow southeastern section of the fault. In addition, the overall depth of the slip concentration in the southeast half of the fault is deeper in the strong-motion model.

To test the compatibility of the teleseismic-waveform and strong-motion data, and to establish a model consistent with both, we performed a combined inversion of both data sets. In the combined inversion, we used the average of the smoothing weights used in the separate inversions. Also, because of the relatively small source dimensions, the near-source strong-motion data have more resolving power than the teleseismic-waveform data, which are dominated by a single velocity pulse that is not as sensitive to subtle changes in the details of the rupture process as are the higher-frequency strong-motion data. Accordingly, we chose to weight the strong-motion data by a factor of 2 over the teleseismic-waveform data in the combined inversion.

The slip distribution resulting from the combined inversion of the strong-motion and teleseismic-waveform data (fig. 12) is nearly identical to that resulting from the

inversion of either data set. This result could have been anticipated because our previous models, which were derived from these independent data sets, are so similar. The combined model, which we prefer, represents a compromise between our two previous source models. To best satisfy both data sets, however, slip is more concentrated

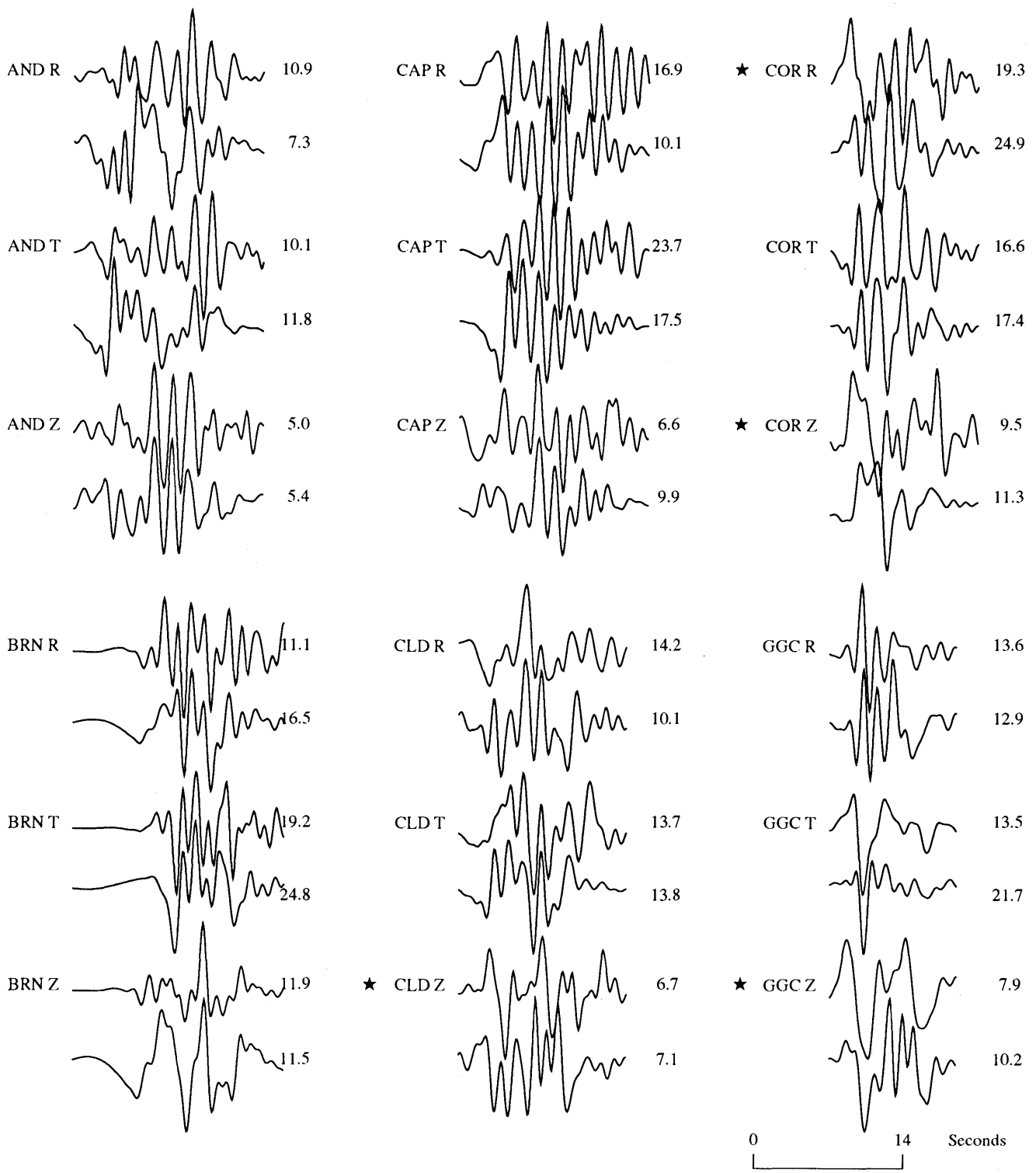

Figure 10.—Comparison of observed (upper curve) and synthetic (lower curve) seismograms of velocity at local-strong-motion stations (see fig. 2 for locations). Number to right of each curve is peak velocity (in centimeters per second). Stars, forward modeling only.

in the central part of the northwest lobe of dislocation, in comparison with the more diffuse slip in the previous models. The matchup of teleseismic waveforms is only slightly degraded, and the strong-motion synthetic seismograms are only slightly affected by the increased smoothing constraints.

FORWARD MODELING OF GROUND MOTION

In this section, we use our finite-fault-source inversion results to characterize ground motions more generally. First, we seek to determine whether the teleseismic-wave-

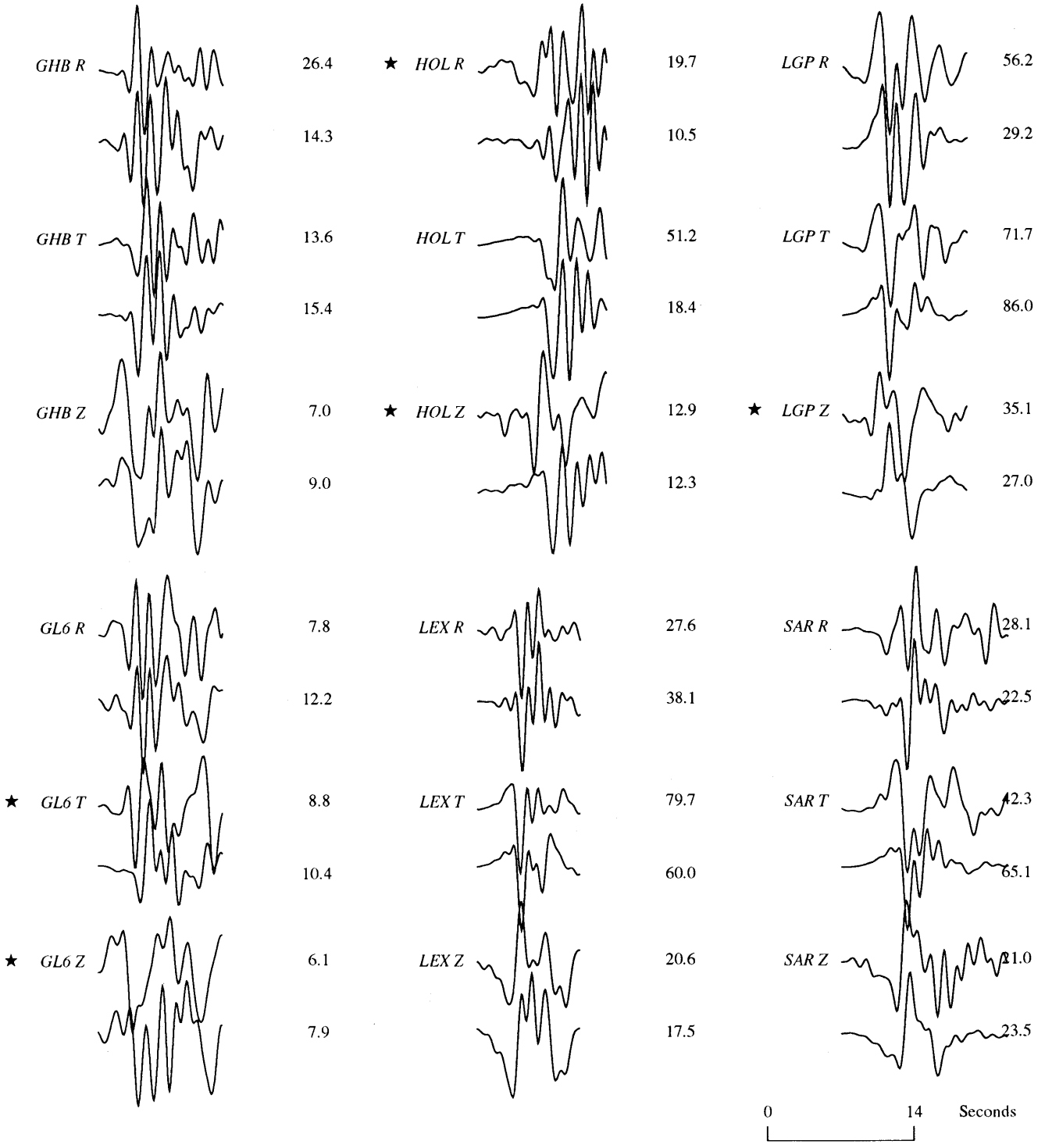

Figure 10.—Continued.

form data alone are sufficient to adequately resolve the source characteristics necessary to predict local strong ground motions. In forward modeling, this hypothesis was tested by predicting the strong motions, using the teleseismically derived source model. We then compared the strong motions predicted by the teleseismic source model with those predicted by the strong-motion source model.

Second, we show that the inversion of strong-motion data is useful for estimating the ground motions over the entire source region. The overall distribution of strong-

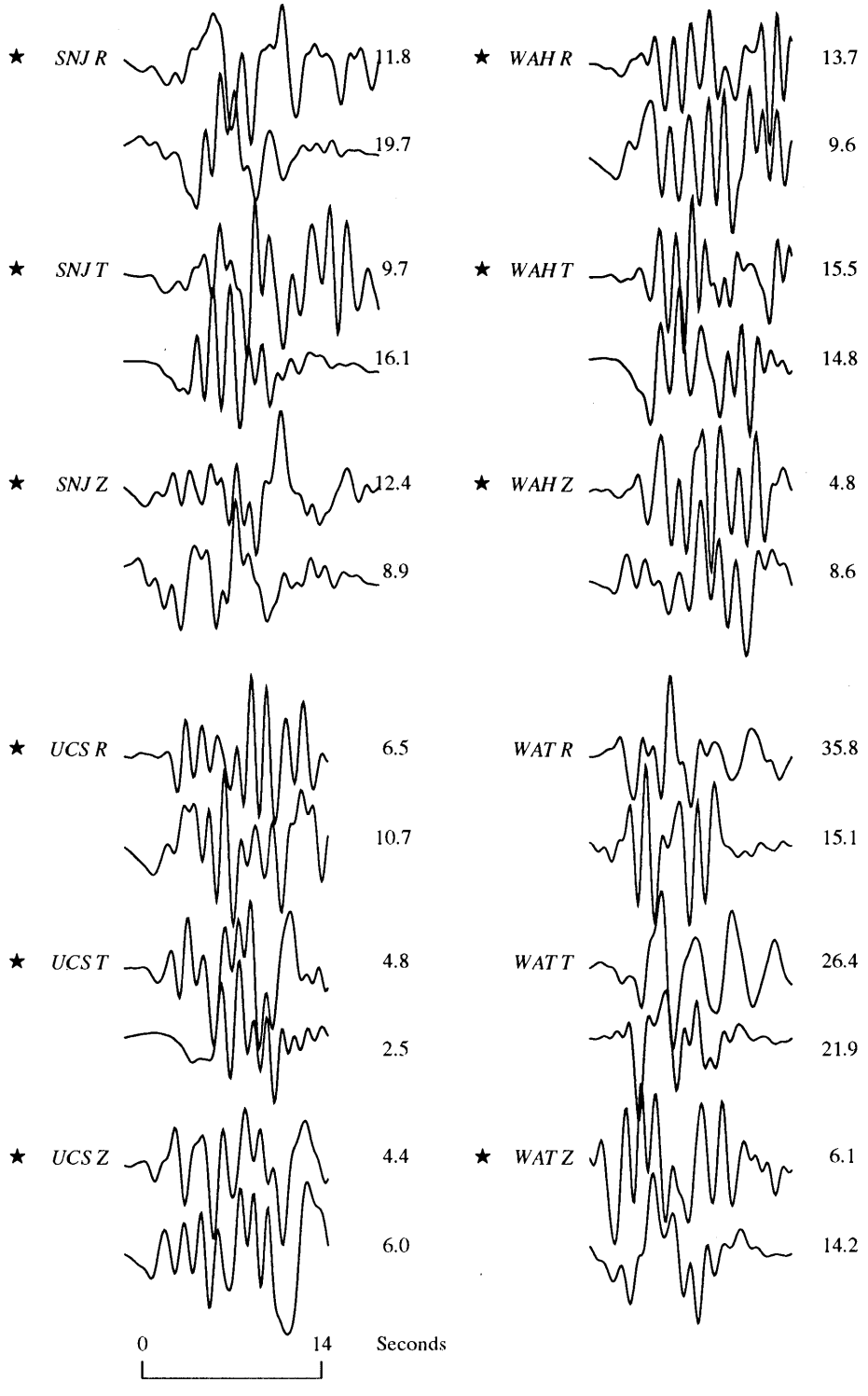

Figure 10.—Continued.

Table 5.—*Inversion model*

["Northwest" and "southeast" refer to halves of the fault. Radius is of asperity used in stress-drop calculations (figs. 12–14). Stress drop is of asperities in northwest and southeast halves of the fault (shading, fig. 12)]

Model	Seismic moment (10^{26} dyne-cm)	Peak slip amplitude (cm)	Radius (km)	Average slip (cm)	Stress drop (bars)
Strong motion:					
Northwest	1.9	350	7.2	209	138
Southeast	1.2	460	6.2	148	114
Total	3.1	460	---	134	46
Teleseismic:					
Northwest	2.0	347	6.3	210	155
Southeast	.8	420	5.8	129	105
Total	2.8	420	---	118	41
Strong motion and teleseismic:					
Northwest	2.2	491	5.3	248	218
Southeast	.8	371	6.2	181	136
Total	3.0	491	---	141	---

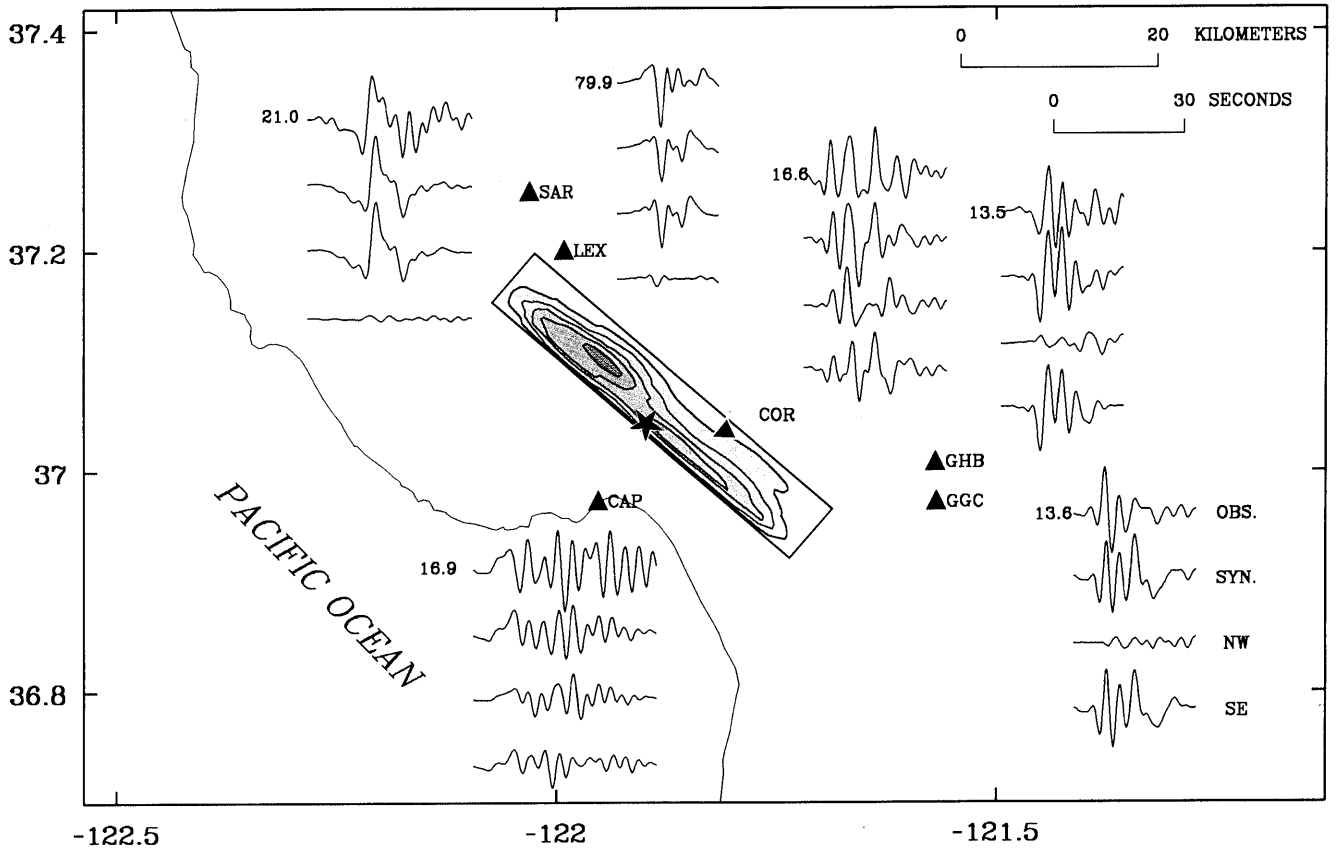

Figure 11.—Loma Prieta region, Calif., showing locations of strong-motion stations (triangles), epicenter of 1989 earthquake (star), and surface projection of model fault plane used in this study (shaded rectangle). Curves represent observed (uppermost) and synthetic (second) seismograms of ground motion, with synthetic contributions from northwest (third) and southeast (lowermost) halves of model fault. Number to left of uppermost curve is common peak velocity to which all curves for each station are scaled.

motion velocities was characterized by predicting ground motions at various sites not represented by strong-motion recordings. In addition, we modified the source-rupture model and analyzed the overall effect of fault geometry and rake on the resulting ground motions. Specifically, we preserved the slip distribution of the strong-motion model, constrained the slip to be strike slip on the adjacent vertical, shallow segment of the San Andreas fault, and then compared the resulting ground motions to those from the dipping, oblique-slip Loma Prieta rupture. This scenario of vertical strike-slip rupture is plausible for a future earthquake on this section of the San Andreas fault, and might be considered a lower bound on the ground motions sustained during the 1906 San Francisco earthquake.

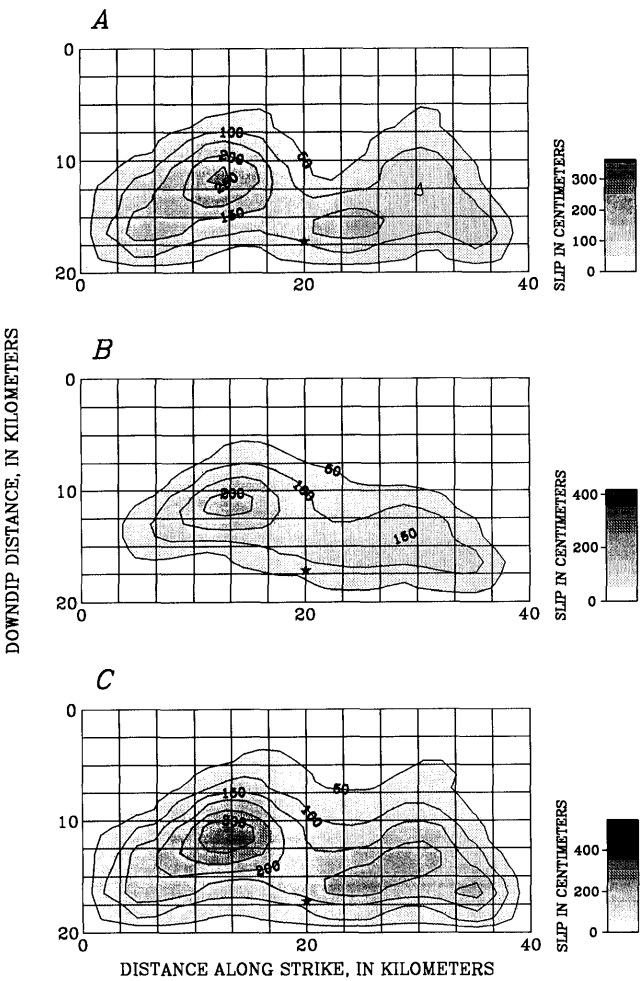

Figure 12.—Northwest-southeast cross section of model fault (fig. 3), showing contours of dislocation for strike slip (*A*), dip slip (*B*), and oblique slip (*C*) predicted from combined inversion of teleseismic-waveform and strong-motion data. Contour interval, 50 cm. Star, hypocenter of 1989 Loma Prieta earthquake.

GROUND-MOTION PREDICTION FROM TELESEISMIC MODEL

Given the rupture model determined from inversion of the teleseismic-waveform data exclusively (fig. 5), it is straightforward to compute the local ground motions at the 16 stations that recorded the strong motions (table 2): We simply replace the strong-motion slip model with the teleseismic slip model and forward-model the resulting ground velocities. Recall that the fault-model parametrization is identical for both the strong-motion and teleseismic-waveform data; only the spatial smoothing and final slip distribution, including the relative weights within each of the three time windows, vary.

We might expect that, given the similarities of the teleseismic model to the strong-motion model (figs. 5, 9), comparable strong motions would be predicted. The observed ground-motion velocities at selected stations are compared with the synthetic waveforms predicted by the strong-motion and teleseismic source models in figure 13. The various stations were chosen as representative of regions above the northwestern, central, and southern sections of the fault. This waveform comparison indicates that the teleseismic synthetic ground motions (lower curve) fit the overall amplitudes and durations of the observed ground motions (upper curve) quite well. We expected the amplitudes and phases of individual arrivals to differ from the strong-motion data, considering that this phase information was omitted from the teleseismic inversion. We note, however, a slightly longer period quality in the teleseismic synthetic ground motions (lower curve) than in the strong-motion synthetic (middle curve) and observed (upper curve) seismograms. This shift to longer periods is noticeable at station LEX (fig. 13).

For a more systematic comparison, we can quantify the misfit to observations for both the strong-motion and teleseismic source models by examining the difference in the response spectra of the observed and synthetic seismograms. We use the methodology of Abrahamson and others (1990) to evaluate the uncertainty in numeric strong-motion predictions as appropriate for engineering applications. We calculate the natural logarithm of the spectral acceleration at 5-percent damping on each horizontal component and then average the spectra for the two horizontal components. As shown by Abrahamson and others (1990), the estimated model bias is given by the mean error, ε, as a function of spectral frequency, f, by the relation:

$$\varepsilon(f) = \frac{1}{N}\sum_{i=1}^{N}(\ln \mathrm{SA}_i^o - \ln \mathrm{SA}_i^s),$$

where SA_i^o is the observed and SA_i^s is the synthetic spectral acceleration for the ith recording, and N is the total number of recordings. We compute the mean error only

for spectral frequencies within the bandpass of the inversion (0.2–1.0 Hz).

The mean error averaged over both horizontal components of all stations, and the 90-percent-confidence interval of the bias for the strong-motion and teleseismic source models, are compared in figure 14. The model is considered unbiased if its bias does not differ significantly from zero at the 90-percent-confidence level (Abrahamson and others, 1990). Over this frequency range, the strong-motion synthetic seismograms show very little bias in comparison with the observed seismograms. This result is not surprising, considering that the solution was determined by using a least-squares fit between the synthetic and observed strong-motion seismograms.

In the teleseismic model, within the 90-percent-confidence interval, the bias differs only marginally from zero. The synthetic seismograms slightly overpredict the velocity at frequencies below 0.4 Hz and underpredict it at higher frequencies. This result indicates, however, that the teleseismic source models, determined independently from the strong-motion data, can be used to predict the near-fault ground motions for comparable earthquakes that might lack strong-motion recordings.

We note that the forward prediction of strong motions from the teleseismic-waveform data is sensitive to the spatial smoothing chosen for the teleseismic model. For this reason, the 1989 Loma Prieta earthquake, with abundant teleseismic-waveform as well as local data, presents a

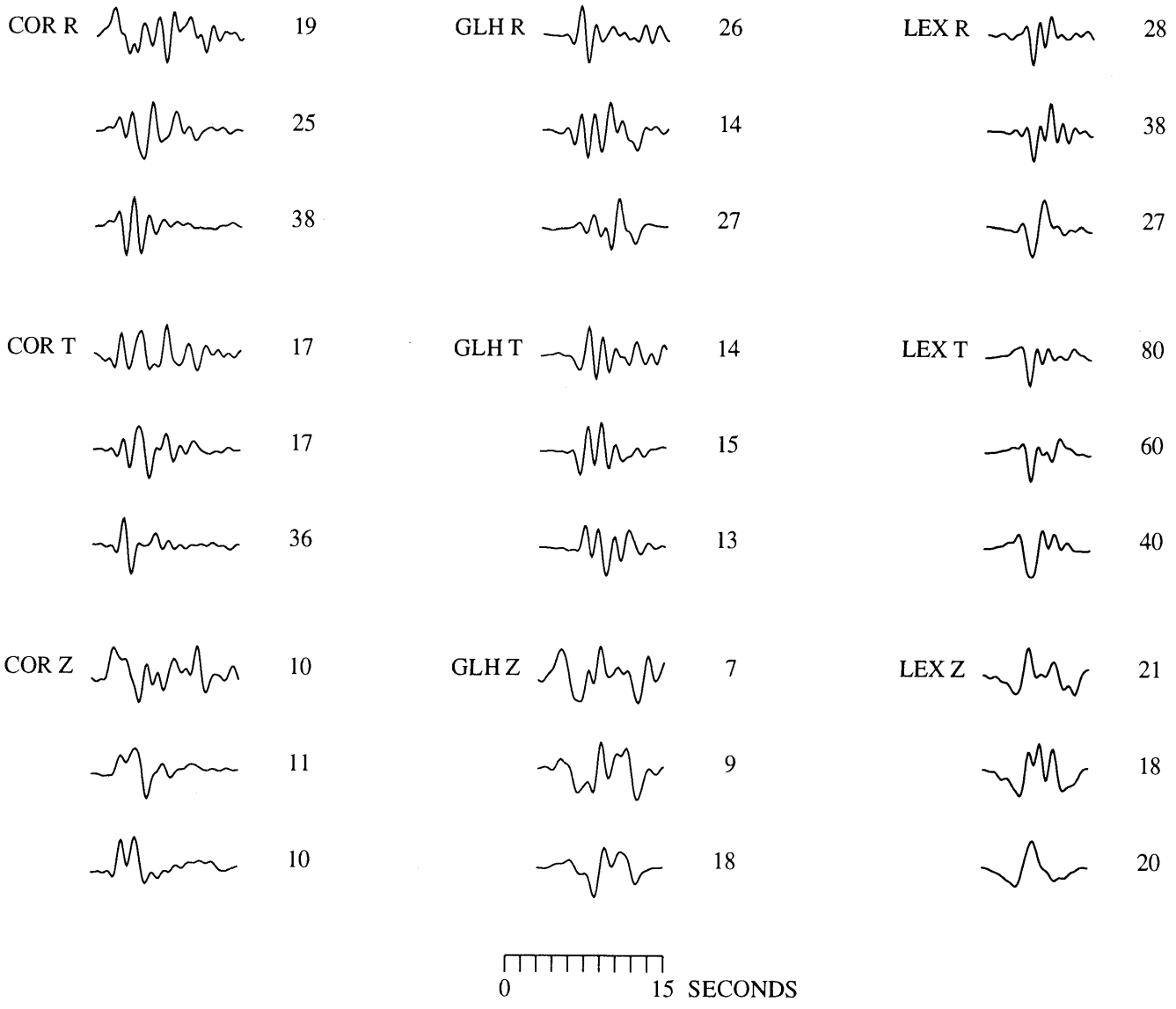

Figure 13.—Comparison of observed seismograms (top curve), synthetic seismograms produced with strong-motion dislocation model (middle curve), and synthetic seismograms produced with teleseismic dislocation model (bottom curve) for radial (R), tangential (T), and vertical (Z) components of velocity at local-strong-motion stations COR, GLH, and LEX (fig. 2). Number to right of curve is peak velocity (in centimeters per second).

unique chance to examine the relation between these parameters. Because inversions of teleseismic-waveform data alone generally tend to prefer solutions with numerous isolated, high-slip subfaults, significant smoothing was required to minimize the variation of slip between adjacent subfaults. Thus, as presented here, the teleseismic-waveform model represents a lower estimate of the fault slip heterogeneity. The net effect is a noticeable underprediction of the higher-frequency (>0.7 Hz) energy, as shown in figure 14, and a slight overprediction of longer-period (<0.4 Hz) energy.

Our estimation of the smoothing required for the teleseismic model appears to be reasonable, considering the sufficient fit to the strong-motion predictions (figs. 13, 14). In our future work, we will more fully examine the relation between the theoretical spatial smoothing used for teleseismic modeling and the effects on estimations of higher-frequency radiation.

ESTIMATED PEAK-GROUND-VELOCITY DISTRIBUTION

The dislocation model derived from inversion of the teleseismic and strong-motion data can also be used to characterize the ground motions at a site anywhere within the source region (fig. 1). For example, Hartzell and Iida (1990) used their rupture model of the 1987 Whittier Narrows, Calif., earthquake, derived from inversion of local strong-motion data, to forward-model the ground motions over the entire epicentral region. In using this approach, we are limited only by the farthest distance to which adequate Green's functions are available. For the Loma Prieta source area, we computed synthetic ground-motion velocities over a grid of stations (crosses, fig. 15), with east-west separations of 9 km and north-south separations of 5 km, at a total of 64 locations in addition to the 16 original station locations (table 2). The peak ground velocity was determined at each gridpoint station, and then these values were contoured over the source area.

Two lobes of high peak velocities are apparent in figure 15, one in the southeastern section of the fault and the other in the northwestern section. The largest-amplitude simulations, more than 70 cm/s, are concentrated above the northwestern section of the fault. These two lobes represent the combined effects of the two asperity depths and locations (fig. 9), together with the source radiation pattern. The oblique mechanism, with an average rake of 142°, favors radiation toward the northwest, even for a uniform slip distribution.

The overall pattern of peak velocities (fig. 15) agrees well with many of the observed indicators of strong ground shaking during the earthquake, confirming that areas above the northwestern section of the fault underwent the strongest shaking. The largest ground velocities were measured at stations (LEX, LGP, SAR, fig. 2) within the northwest lobe of large computed ground motions. Furthermore, the MMI map of Stover and others (1990) (fig. 2*C*) shows a localized concentration of MMI VIII observations within the northwest lobe of large computed ground motions. This area of the southern Santa Cruz Mountains was also where most ground ruptures and fissures formed during the earthquake, particularly along Summit Road and Skyline Ridge. Ponti and Wells (1991) attributed these

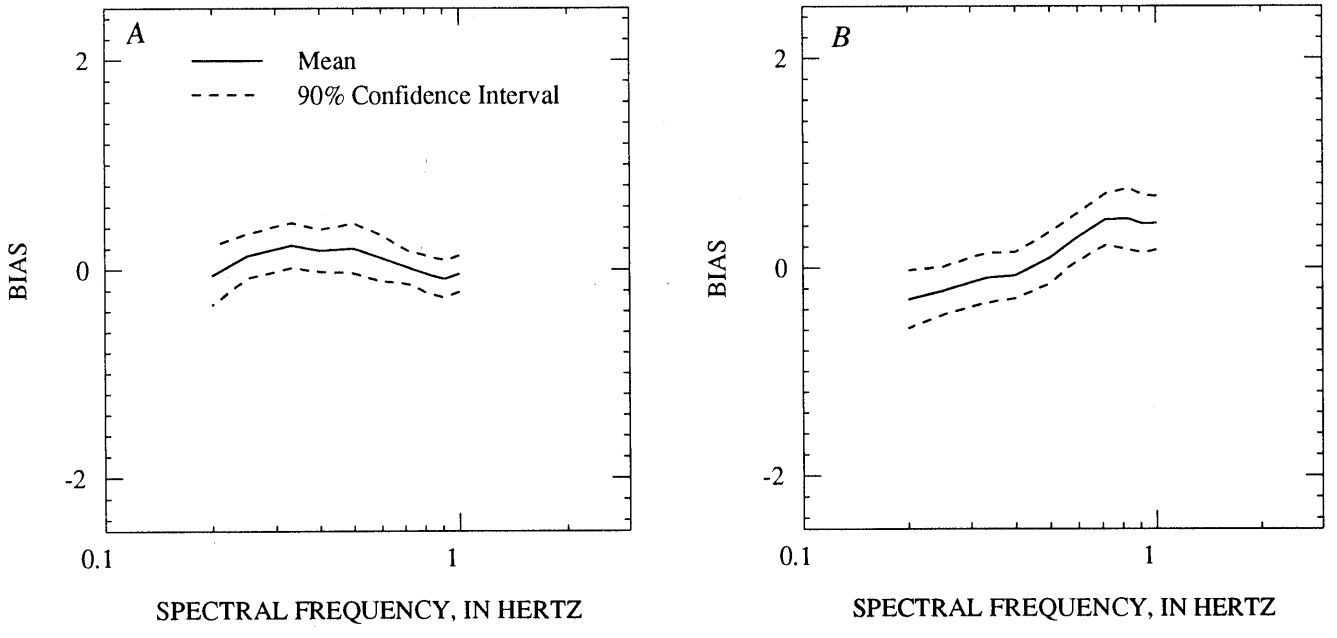

Figure 14.—Bias and 90-percent-confidence interval of bias versus spectral frequency for strong-motion inversion (*A*) and teleseismic inversion (*B*).

displacements to shaking-induced gravitational spreading of ridges and downslope movement, and noted that the greatest damage to competent structures and the highest concentration of topped trees, displaced boulders, and seismically activated landslides were in this area.

Finally, to further characterize the ground-motion hazards in this area, we modified the strong-motion rupture model to simulate a vertical strike-slip rupture along the San Andreas fault with a comparable slip distribution to the Loma Prieta strong-motion model. By rotating the model fault to a vertical plane and constraining the dislocation to be pure right-lateral strike slip, we approximate rupture along the San Andreas fault. For consistency with the average depth of significant slip from other strong-motion waveform inversions of California vertical strike-slip earthquakes (Hartzell and Heaton, 1983; Beroza and Spudich, 1988; Wald and others, 1990), we needed to decrease the asperity depth relative to the Loma Prieta model fault by bringing the top of the fault to within 0.5 km of the surface and translating the slip (see fig. 9) 5 km closer to the top of the fault (fig. 16). The strike was kept identical to that in the Loma Prieta model, causing a minor discrepancy in the strike of the model fault (straight line, fig. 17) relative to the strike of the San Andreas fault. The absolute amplitude of slip was preserved, resulting in a slightly smaller total seismic moment (owing to the reduced rigidity at the depths of the shallower slip). The slight difference in the contours (compare figs. 9 and 16) results from compressing the fault width over which slip occurs.

The overall pattern of the resulting peak ground velocities computed with the vertical strike-slip-fault model (fig. 16) is shown in figure 17. Note that the overall velocities are higher than in the Loma Prieta model. These higher velocities are attributable to the relatively shallow slip relative to the Loma Prieta model. Note that the asperity toward the northwestern section of the fault is shallower than that toward the southeastern section (fig. 16), suggesting that near-source ground motions during the earthquake were moderated by the relatively large average depth of significant slip.

DISCUSSION

We have presented our slip models by using contour maps that are spatially smoothed to deemphasize the abrupt subfault boundaries used in our inversion scheme. To com-

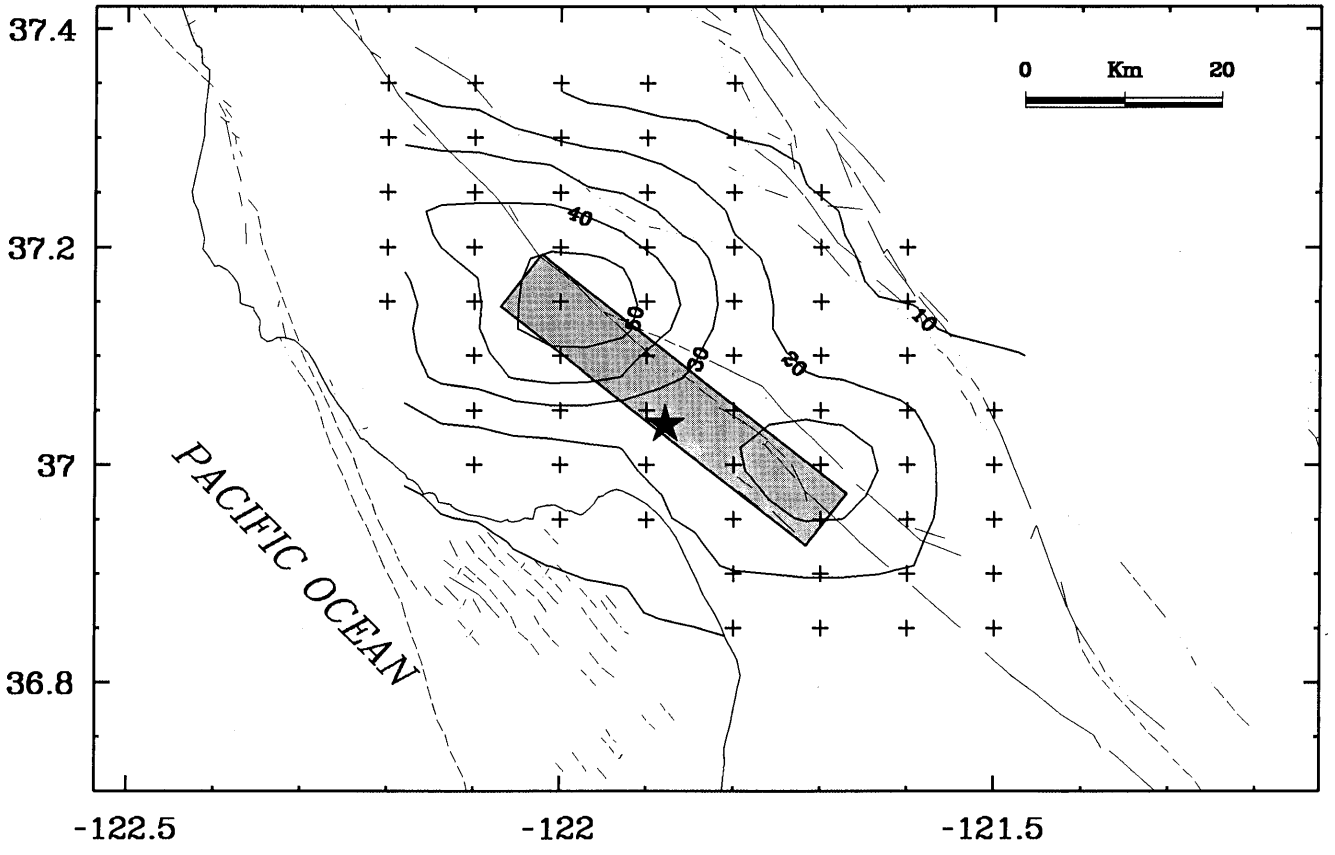

Figure 15.—Loma Prieta region, Calif., showing epicenter of 1989 earthquake (star), surface projection of model fault plane used in this study (shaded rectangle), and contours of peak ground velocity predicted from strong-motion source model. Contour interval, 10 km/s. Crosses, grid of stations used in forward modeling.

pare our inversion models in more detail, the slip vectors for individual subfaults are shown in figure 18, and the maximum absolute slip amplitudes are listed in table 5. The average rake angles, based on the relative components of strike slip and dip slip for the strong-motion, teleseismic, and combined inversions are 142°, 144°, and 145°, respectively, in agreement with the range of values reported in teleseismic point-source studies by other researchers and with the geodetic modeling results (Lisowski and others, 1990).

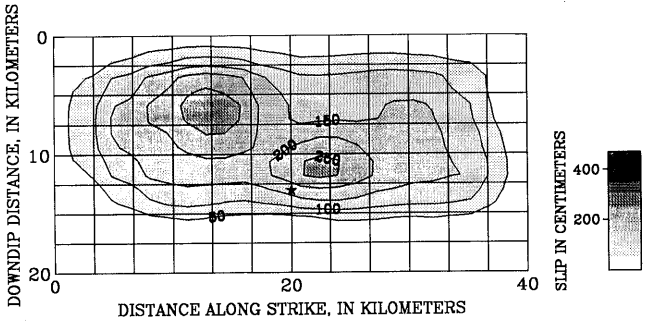

Figure 16.—Northwest-southeast cross section of model fault (fig. 3), showing contours of dislocation for vertical strike slip predicted from strong-motion model. Contour interval, 50 cm. Star, hypocenter of 1989 Loma Prieta earthquake.

Although inversion of only the teleseismic-waveform data does not result in systematic spatial variations of the rake angle (fig. 18*B*), inversion of the strong-motion data (figs. 18*A*, 18*C*) shows a clear tendency for more nearly vertical rake angles of slip to the northwest of the hypocenter and more nearly horizontal rake angles of slip to the southeast. Although our model assumes that all slip occurs on a single, 70°-dipping plane, this systematic change in rake angle coincides with an apparent change in dip of the aftershock zone from about 70° for the segment northwest of the hypocenter to nearly vertical near the southeast edge of the fault plane (Dietz and Ellsworth, 1990).

One shortcoming of our model is its failure to predict the large transverse motions observed at station HOL (fig. 10), although site-response studies indicate significant site amplifications at this station (Keiiti Aki, written commun., 1991). Station HOL, which is located along the southeastward projection of the fault, has an unusually large motion perpendicular to the fault strike (fig. 2*B*). This

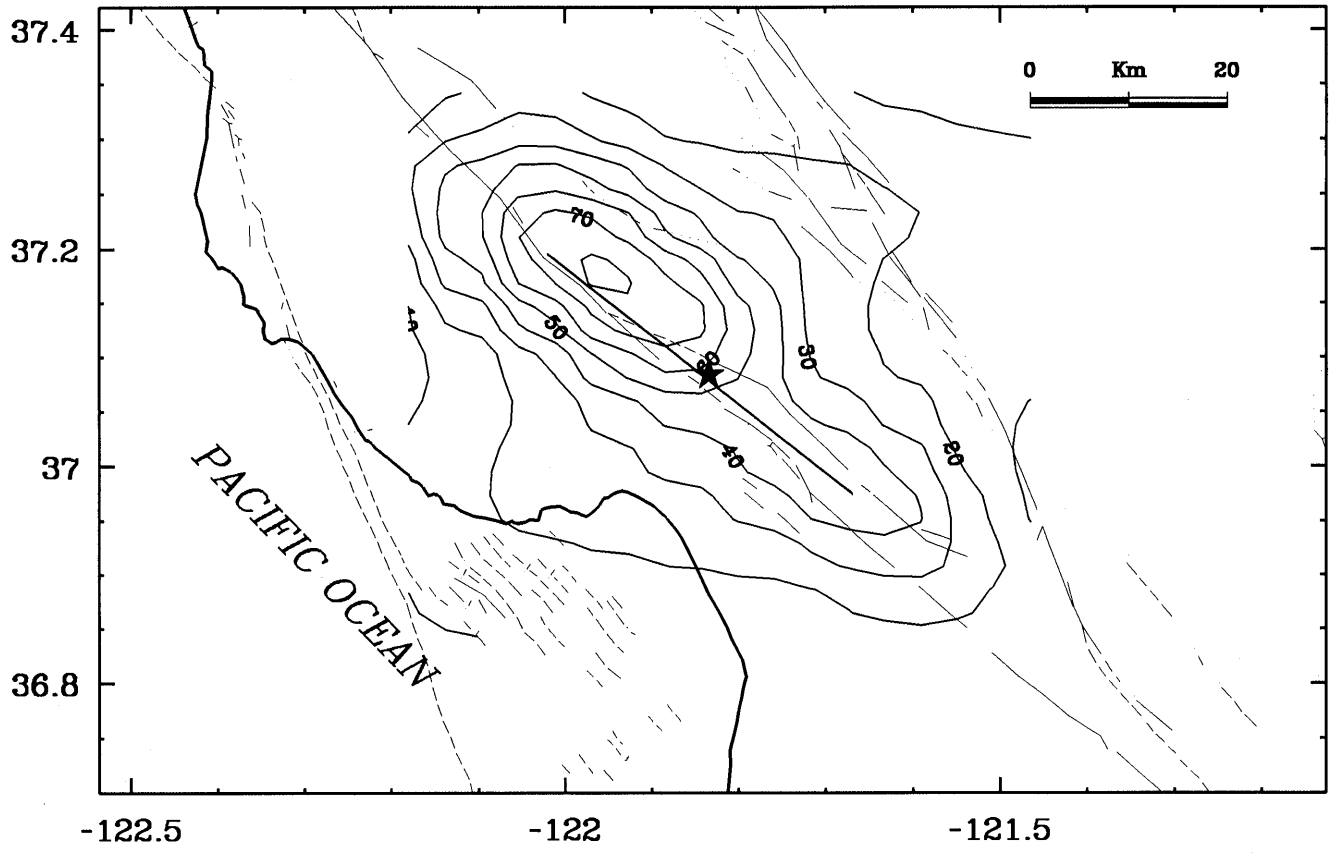

Figure 17.—Loma Prieta region, Calif., showing predicted contours of peak ground velocity from a vertical strike-slip rupture along the San Andreas fault, based on 1989 Loma Prieta slip distributions. Contour interval, 10 cm/s. Irregular thin lines, faults (dashed where inferred), digitized from major Quaternary faults mapped by Jennings (1975); straight line, model fault length; star, epicenter of 1989 Loma Prieta earthquake.

waveform suggests strike-slip faulting on a separate, vertically dipping, southeast-trending fault plane at the southeast end of the aftershock area (possibly the San Andreas fault). The radiation pattern from a vertical strike-slip mechanism would greatly enhance the tangential component and yet not contribute to the near-nodal radial and vertical components. Such a model is consistent with the near-vertical aftershock distribution and strike-slip mechanisms near the southeast edge of the inferred rupture zone (Dietz and Ellsworth, 1990). Although a minor amount of pure strike-slip motion occurs on the shallow southeastern section of our model fault inferred from the teleseismic-waveform data (2.5–7.5 km downdip, 23–36 km along strike; fig. 18), such motion is not seen in models inferred from the strong-motion data.

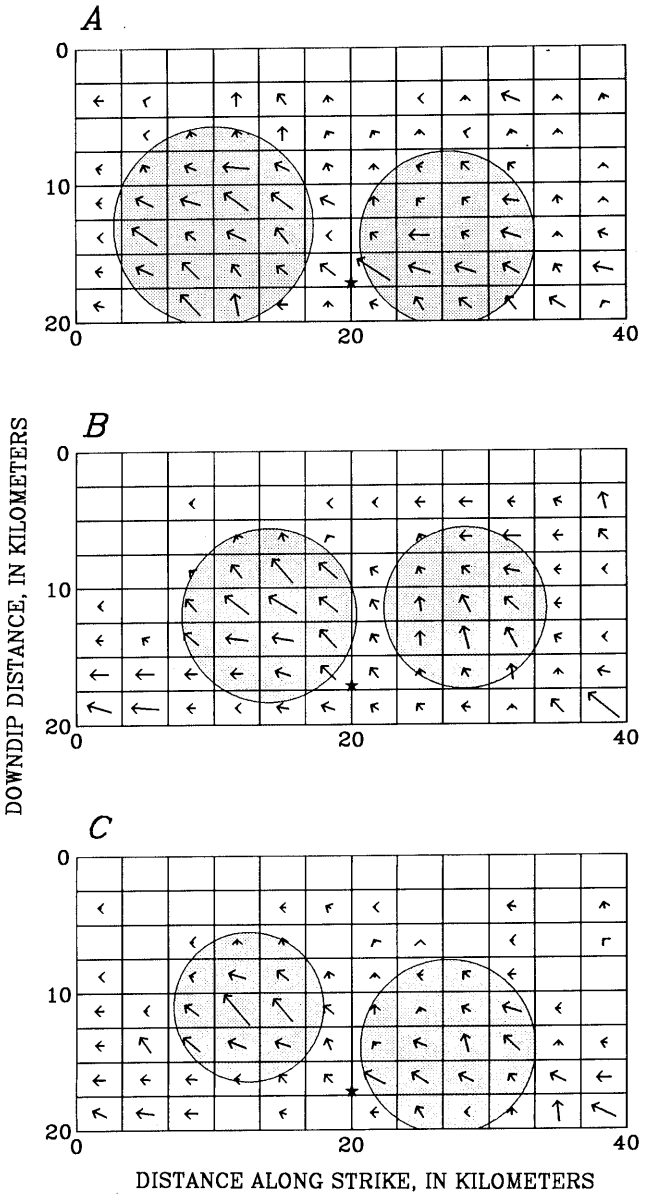

Figure 18.—Northwest-southeast cross section of model fault (fig. 3), showing rake angle (vector) for each subfault as determined from inversion of strong-motion (*A*) and teleseismic (*B*) data sets, and from combined inversion of both data sets (*C*). Length of each vector is normalized to peak slip on model fault plane. Shaded circles, patches where most slip is concentrated; star, hypocenter of 1989 Loma Prieta earthquake.

To estimate the stress drop for the regions of concentrated slip, we approximate their area with a circle and calculate the average slip amplitude within that circle (shaded circles, fig. 18). Using the stress-drop relation of Eshelby (1957) for a circular fault, $\Delta\sigma=7\pi\mu\bar{u}/16a$, where μ is the rigidity (3.4×10^{11} dyne/cm^2), $\bar{u}$ is the average dislocation, and a is the radius, we obtain the stress drops listed in table 5. For the entire fault rupture, the relation of Parsons and others (1988) is more appropriate for a long, buried strike-slip fault: $\Delta\sigma=C\mu\bar{u}/w$, where w is the downdip fault width and C is a constant dependent on the fault-plane dimensions. Using our fault dimensions, their results require that $C\simeq1.75$. Setting w=17 km, we obtain the stress drops for all three inversions listed in table 5.

In general, the rupture dimensions of significant slip agree well with the overall slip dimensions based on the active perimeter of the aftershock zone (Dietz and Ellsworth, 1990). This result is consistent with the observation of Mendoza and Hartzell (1988) that aftershocks commonly cluster along the margin of fault regions that underwent large coseismic slips. The regions of major slip in our model coincide with a region of relatively few aftershocks in the central part of the aftershock zone, although our model suggests less updip rupture than that inferred by Dietz and Ellsworth (1990) from the aftershock distribution alone. Thus, whereas the general features of the rupture can generally be inferred from aftershock activity, significant features of the rupture may be obscured in the aftershock patterns. The exact details of the aftershock pattern from the earthquake vary significantly, depending on the time period chosen for the analysis (for example, Dietz and Ellsworth, 1990, figs. 3a–3c). Therefore, we consider only larger (M>4.0) aftershocks, including those within the first 34 minutes after the main shock (Simila and others, 1990), and find that they tend to cluster around the major slip concentrations in our model (fig. 9*C*), particularly in the northwestern section of the fault.

The use of three time windows (each of 0.7 s) allows several general observations about the rupture-velocity and slip-time history. We expect regions requiring a locally lower rupture velocity to make use of the later time windows so as to compensate for the lower, fixed rupture velocity. Likewise, regions with a higher rupture velocity would take advantage of only the first rupture window. Overall, in both the strong-motion and teleseismic inversions, slip in time window 1 dominates, and only minor slip occurs in time windows 2 and 3 (fig. 19) over much of the fault. This result implies that the rupture timing in

our model satisfies the data and that large variations in rupture velocity are unnecessary. In addition, a locally lower rupture velocity or somewhat longer slip duration may be evident along the outer northwestern margin of the northwestern asperity, in the same region where most M>4.0 aftershocks occurred.

The concentration of most slip in time window 1 indicates that short slip durations (<1 s) are preferred in our model at a given point on the fault, implying that only a small part of the entire rupture surface is slipping at any given time. For example, the section of the fault rupturing 5 s after the nucleation time in figure 3 is shown as the shaded area within time window 1. Short slip durations, which have also been inferred for other earthquakes, have an important implications for rupture mechanics (Heaton, 1990).

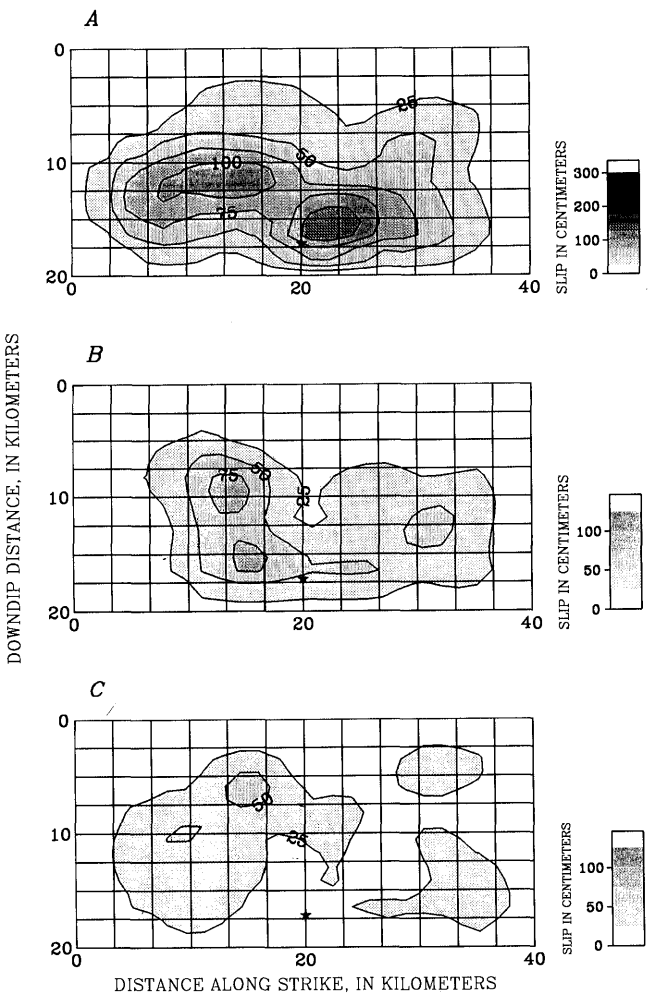

Figure 19.—Northwest-southeast cross section of model fault (fig. 3), showing contours of oblique slip predicted from strong-motion inversion for time windows 1 (*A*), 2 (*B*), and 3 (*C*). Contour interval, 50 cm. Star, hypocenter of 1989 Loma Prieta earthquake.

CONCLUSIONS

From our analysis of the three inversions, we find a bilateral dislocation pattern, with two main regions of oblique slip: the first centered about 6 to 8 km northwest of the hypocenter at 11- to 13-km depth and the other centered at 7 to 9 km southeast of the hypocenter at 15- to 16-km depth. The northwestern patch, which has a larger seismic moment, a larger average slip amplitude, and thus a higher overall stress drop (table 5), is the source of the largest observed strong-motion velocities, recorded about 20 km northwest of the epicenter (see figs. 2, 11). Dominant radiation toward the northwest is also confirmed by the overall damage patterns and landslides concentrated in areas northwest of the epicenter (Benuska, 1990). Likewise, an azimuthal dependence in the peak ground motions was observed by Boore and others (1989) (see fig. 6), who noted a tendency for high residuals relative to predicted peak velocities at rock sites toward the northwest relative to all other azimuths.

We now compare our slip model with the other finite-fault dislocation models for this earthquake (Beroza, 1991; Hartzell and others, 1991; Steidl and others, 1991). Although significant differences in the amplitude and direction of slip vectors exist between our model and the others, they all agree remarkably well on the overall characteristics of this rupture. All researchers conclude that a bilateral rupture with relatively low slip updip from the hypocenter best explains the waveforms, and researchers find that most slip occurred on two relatively small patches nearly equidistant from the hypocenter, one to the northwest and the other to the southeast. All studies indicate that a fairly uniform rupture velocity of approximately 80 percent of the local shear-wave velocity, together with a relatively short slip duration at any point ($\lesssim$1.5 s) best explains the observed waveforms.

Although our model is similar in most respects to the others presented in this chapter, it differs substantially in two aspects. First, the local rake vectors vary significantly among the models discussed below. On average, the rake vectors of about 145° in the area southeast of the hypocenter agree between our model and that of Hartzell and others (1991). Both of these models have similar oblique rake components in the northwestern asperity. In contrast, the southeastern asperity in the models of Beroza (1991) and Steidl and others (1991) shows rake angles indicating nearly pure strike slip (rake, ~160°–170°, yet they have almost pure thrusting rake vectors (80°–90°) within the northwestern asperity. These two models require an approximately 80° change in rake vector from the south half to the north half of the fault and no corresponding change in dip. We emphasize that, although the slip distributions of Beroza (1991) and Hartzell and others (1991) look similar, the rake vector in the region of dominant slip for these models (the southeastern asperity) differs by about

40° and would likely produce substantially different near-field ground motions.

Second, in addition to variation in the local rake directions, the partitioning of total slip along strike in asperities northwest and southeast of the epicenter in our model requires more slip in the northwestern asperity (figs. 5, 9, 18; table 5); the other models require most of the slip in the southeastern asperity. Considering that rise times, rupture velocities, and source geometries are similar among the various models, disparities in the resulting slip distribution most likely reflect variations in the data sets employed. Other parameters being comparable, station coverage and weighting may be the most critical elements controlling the slip partitioning. A source of dominant radiation northwest of the epicenter is required by the strong-motion data used in our study (see fig. 2). In particular, the large coherent arrivals at stations SAR, LEX, and LGP require significant slip and directivity. A comparison of the waveform fits at station SAR by the various models is particularly revealing and reflects the differences in modeling strategy.

The strategy adopted by Steidl and others (1991) was to obtain the largest possible azimuthal coverage by including stations out to 60 km. Thus, they modeled several distant stations to the north quite well, while doing a relatively poor job in fitting both waveform and amplitude at station SAR (fig. 2). They did not use stations LEX and LGP, which recorded the largest ground velocities, and so the wavefield at these ray parameters is downweighted relative to distant samples. If their Green's functions are adequate for these distant stations and ours prove less than desirable at stations LEX, SAR, and LGP, then they have a more reasonable interpretation. A detailed study of aftershock recordings at the various stations is one way to resolve this particular issue, because local receiver structures can be recognized and the adequacy of the theoretical Green's functions may be examined.

It is not so clear why the slip distribution of Beroza (1991) differs from ours. Although he did not use the vertical components of ground motion, his station selection in the northwestern section of the fault is similar to that in our study. Waveforms fits at his northwestern stations, however, show significant differences from those of our model. The differences in slip distribution may partly be due to differences in the applied Green's functions, as he suggested; we used the complete layered-space solutions, whereas he used only geometric-ray approximations. Again, a comparison of near- and far-field Green's functions with simple aftershocks at stations SAR and other stations should help resolve this issue.

Slip in the southeastern asperity is evidently constrained by the southeastern stations, as described in figure 11. We used station WAT (fig. 2) and a few of the Gilroy array stations. We observed that the other Gilroy array stations have complex receiver functions, and so we omitted these stations from our analysis. The data sets used in the other studies excluded station WAT and included additional stations from the Gilroy array. The use of a dense set of stations over limited distance and azimuthal ranges provides redundant coverage and may favor slip in the southern section of the fault.

Clearly, the teleseismic-waveform data have less resolving power along strike than the strong-motion data, as shown by comparison of the *P* and *SH* waveforms from this study and those of Hartzell and others (1991). Although the slip models differ considerably and are nearly northwest-southeast reversed, they produce nearly identical teleseismic waveforms, suggesting an absence of resolution from this data set. The teleseismic-waveform data, however, resolve updip directivity and require a bilateral rupture with little updip slip. Again, the differences in the teleseismic source models probably result from variations in station coverage. Hartzell and others (1991) used similar teleseismic stations to ours but added several additional stations, particularly in the northwestern and northeastern azimuths. These additional stations, however, do not substantially augment azimuthal coverage and may actually bias the results. Removal of these stations from their inversion results in a model similar to ours, favoring northwestern slip (S.H. Hartzell, oral commun., 1990).

We note that even though the slip distribution and rake vectors vary, the net result of any of these models will be nearly the same at long periods. This similarity can be explained by the fact that the bilateral rupture radiates from both asperities simultaneously. Thus, as long as the net rake vector and total seismic moment are preserved, the resulting models should produce similar and adequate teleseismic-waveform matches, though not necessarily for the near-field data. That the waveform comparisons for all the strong-motion models are less than remarkable may reflect the need for a more complex rupture surface than the idealized flat-planar models used here.

In general, the rupture process of the 1989 Loma Prieta earthquake was fairly simple for an M=7.1 earthquake, rupturing only a relatively short (<35 km long) fault segment (Kanamori and Satake, 1990). The relatively short duration of strong motion is partly attributable to the bilateral rupture. Furthermore, the relatively great depth of slip concentrations moderated the amplitude of ground velocities in the near-source region.

Most of our current knowledge of fault-asperity characteristics has been derived from ground-motion frequencies lower (<1 Hz) than the frequency range of most interest in earthquake engineering. Wald and others (1987, 1988) found that large-scale asperity models derived from longer-period velocity data also explained many characteristics of the higher-frequency accelerograms. Our results here indicate that the asperities which control

broadband teleseismic waveforms (3–30 s) also dominate higher-frequency strong motions (1–5 s).

In an effort to understand the radiation of the higher-frequency motions during the 1989 Loma Prieta earthquake, we performed an inversion with the observed and synthetic seismograms bandpass filtered from 0.1 to 3 Hz. We used a finer discretization of the fault plane into 200 subfaults, each with dimensions of 2.0 km along strike and 2.0 km downdip. We also reduced the duration of the source-time function to 0.5 s. Our results indicate that the same regions of large slip which control the longer-period teleseismic waveforms and the strong-motion velocities as high as 1 Hz are also responsible for higher-frequency (>1.0 Hz) radiation. We also note that the inversion using higher-frequency data appears to favor slightly more concentrated asperities. Understanding the relation between long-period source models of large earthquakes and the radiation of high frequencies is critical for a prediction of ground motions in the frequency range of engineering interest. Our future work will address the characteristics of the high-frequency radiation further. Such study will require more sophisticated timing corrections based on the aftershock data recorded at many of the strong-motion stations used here, as well as a more detailed treatment of the variations in propagation paths and site effects at individual stations.

ACKNOWLEDGMENTS

This work was supported by the U.S. Geological Survey under contracts 14–08–0001–21912 and 14–08–0001–G1832. Reviews by Hiroo Kanamori, Paul Somerville, Paul Spudich, and Lisa Wald improved the manuscript. We thank Steve Hartzell for useful discussions and advice on the use of his inversion software, and Norm Abrahamson and Nancy Smith for providing programs to compute the response-spectral bias.

REFERENCES CITED

Abrahamson, N.A., Somerville, P.G., and Cornell, C.A., 1990, Uncertainty in numerical strong motion predictions: U.S. National Conference on Earthquake Engineering, 4th, Palm Springs, Calif., 1990, Proceedings, v. 1, p. 407–416.

Archuleta, R.J., 1984, A faulting model for the 1979 Imperial Valley, California, earthquake: Journal of Geophysical Research, v. 89, no. B6, p. 4559–4585.

Benuska, Lee, ed., 1990, Loma Prieta earthquake reconnaissance report: Earthquake Spectra, v. 6, supp. 90–01, 448 p.

Beroza, G.C., 1991, Near-source modeling of the Loma Prieta earthquake; evidence for heterogeneous slip and implications for earthquake hazards: Seismological Society of America Bulletin, v. 81, no. 5, 81, p. 1603–1621.

Beroza, G.C., and Spudich, Paul, 1988, Linearized inversion for fault rupture behavior; application to the 1984 Morgan Hill, California, earthquake: Seismological Society of America Bulletin, v. 93, no. B6, p. 6275–6296.

Boore, D.M., Seekins, L.C., and Joyner, W.B., 1989, Peak accelerations from the 17 October 1989 Loma Prieta earthquake: Seismological Research Letters, v. 60, no. 4, p. 151–166.

Choy, G.L., and Boatwright, John, 1990, Source characteristics of the Loma Prieta, California, earthquake of October 18, 1989 from global digital seismic data: Geophysical Research Letters, v. 17, no. 8, p. 1183–1186.

Dietz, L.D., and Ellsworth, W.L., 1990, The October, 17, 1989, Loma Prieta, California, earthquake and its aftershocks; geometry of the sequence from high-resolution locations: Geophysical Research Letters, v. 17, no. 9, p. 1417–1420.

Eshelby, J.D., 1957, The determination of the elastic field of an ellipsoidal inclusion, and related problems: Royal Society of London Proceedings, ser. A, v. 241, no. 1226, p. 376–396.

Futterman, W.I., 1962, Dispersive body waves: Journal of Geophysical Research, v. 67, no. 13, p. 5279–5291.

Hartzell, S.H., and Heaton, T.H., 1983, Inversion of strong ground motion and teleseismic waveform data for the fault rupture history of the 1979 Imperial Valley, California, earthquake: Seismological Society of America Bulletin, v. 73, no. 6, pt. A, p. 1553–1583.

———1986, Rupture history of the 1984 Morgan Hill, California, earthquake from the inversion of strong motion records: Seismological Society of America Bulletin, v. 76, no. 3, p. 649–674.

Hartzell, S.H., and Iida, Mashiro, 1990, Source complexity of the 1987 Whittier Narrows, California, earthquake from inversion of strong motion records: Journal of Geophysical Research, v. 95, no. B8, p. 12475–12485.

Hartzell, S.H. and Mendoza, Carlos, 1991, Application of an iterative least-squares waveform inversion of strong motion and teleseismic records to the 1978 Tabas, Iran, earthquake: Seismological Society of America Bulletin, v. 81, no. 2, p. 305–331.

Hartzell, S.H., Stewart, G.S., and Mendoza, Carlos, 1991, Comparison of L_1 and L_2 norms in a teleseismic inversion for the slip history of the Loma Prieta, California, earthquake: Seismological Society of America Bulletin, v. 81, no 5, p. 1518–1539.

Heaton, T.H., 1982, The 1971 San Fernando earthquake; a double event?: Seismological Society of America Bulletin, v. 72, no. 6, p. 2037–2062.

———1990, Evidence for and implications of self-healing pulses of slip in earthquake rupture: Physics of the Earth and Planetary Interiors, v. 64, no. 1, p. 1–20.

Heaton, T.H., and Heaton, R.E., 1989, Static deformations from point forces and force couples located in welded elastic Poissonian half-spaces; implications for seismic moment tensors: Seismological Society of America Bulletin, 79, no. 3, p. 813–841.

Jennings, C.W., compiler, 1975, Fault map of California, with locations of volcanoes, thermal springs, and thermal wells: California Division of Mines and Geology Geologic Data Map 1, scale 1:750,000.

Kanamori, Hiroo, and Satake, Kenji, 1990, Broadband study of the 1989 Loma Prieta earthquake: Geophysical Research Letters, v. 17, no. 8, p. 1179–1182.

King, G.C.P., Lindh, A.G., and Oppenheimer, D.H., 1990, Seismic slip, segmentation, and the Loma Prieta earthquake: Geophysical Research Letters v. 17, no. 9, p. 1449–1452.

Langston, C.A., and Helmberger, D.V., 1975, A procedure for modelling shallow dislocation sources: Royal Astronomical Society Geophysical Journal, v. 42, no. 1, p. 117–130.

Lisowski, Michael, Prescott, W.H., Savage, J.C., and Johnston, M.J.S., 1990, Geodetic estimate of coseismic slip during the 1989 Loma Prieta, California, earthquake: Geophysical Research Letters, v. 17, no. 9, p. 1437–1440.

Maley, R.P., Acosta, A.V., Ellis, F., Etheredge, E.C., Foote, L.J., Johnston, D.A., Porcella, R.L., Salsman, M.J., and Switzer, J.C., 1989, U.S. Geological Survey strong-motion records from the north-

ern California (Loma Prieta) earthquake of October 17, 1989: U.S. Geological Survey Open-File Report 89–568, 85 p.

Mendoza, Carlos, and Hartzell, S.H., 1988, Aftershock patterns and main shock faulting: Seismological Society of America Bulletin, v. 78, no. 4, p. 1438–1449.

Olson, A.H. and Apsel, R.J., 1982, Finite faults and inverse theory with application to the 1979 Imperial Valley earthquake: Seismological Society of America Bulletin, v. 72, no. 6, p. 1969–2001.

Olson, A.H., Orcutt, J.A., and Frazier, G.A., 1984, The discrete wave number/finite element method for synthetic seismograms: Royal Astronomical Society Geophysical Journal, v. 77, no. 2, p. 421–460.

Olson, J.A., 1990, Seismicity in the twenty years preceding the Loma Prieta, California earthquake: Geophysical Research Letters, v. 17, no. 9, p. 1429–1432.

Oppenheimer, D.H., 1990, Aftershock slip behavior of the 1989 Loma Prieta, California earthquake: Geophysical Research Letters, v. 17, no. 8, p. 1199–1202.

Parsons, I.D., Hall, J.F., and Lyzenga, G.A., 1988, Relationships between the average offset and the stress drop for two- and three-dimensional faults: Seismological Society of America Bulletin, v. 78, no. 2, p. 931–945.

Ponti, D.J., and Wells, R.E., 1991, Off-fault ground ruptures in the Santa Cruz Mountains, California; ridge-top spreading versus tectonic extension during the 1989 Loma Prieta earthquake: Seismological Society of America Bulletin, v. 81, no. 5, p. 1480–1510.

Schwartz, S.Y., Orange, D.L., and Anderson, R.S., 1990, Complex fault interactions in a restraining bend on the San Andreas Fault, southern Santa Cruz Mountains, California: Geophysical Research Letters, v. 17, no. 9, p. 1207–1210.

Seeber, Leonardo, and Armbruster, J.G., 1990, Fault kinematics in the 1989 Loma Prieta rupture area during 20 years before that event: Geophysical Research Letters, v. 17, no. 9, p. 1425–1428.

Shakal, A.F., Huang, M.J., Reichle, Michael, Ventura, C.E., Cao, T.Q., Sherburne, R.W., Savage, M., Darragh, R.B., and Petersen, C., 1989, CSMIP strong-motion records from the Santa Cruz Mountains (Loma Prieta), California earthquake of 17 October 1989: California Division of Mines and Geology, Office of Strong Motion Studies Report OSMS 89–06, 196 p.

Simila, G.W., McNally, K.C., Nava, E., Protti-Quesada, M., and Yellin, Joseph, 1990, Evidence of very early aftershock activity along the northwest portion of the 18 October 1989 earthquake rupture zone: Geophysical Research Letters, v. 17, no. 10, p. 1785–1788.

Steidl, J.H., Archuleta, R.J., and Hartzell, S.H., 1991, Rupture history of the 1989 Loma Prieta, California, earthquake: Seismological Society of America Bulletin, v. 81, no. 5, p. 1573–1602.

Stover, C.W., Reagor, B.G., Baldwin, F.W., and Brewer, L.R., 1990, Preliminary isoseismals map for the Santa Cruz (Loma Prieta), California, earthquake of October 18, 1989 UTC: U.S. Geological Survey Open-File Report 90–18, 24 p.

U.S. Geological Survey staff, 1990, The Loma Prieta, California, earthquake; an anticipated event: Science, v. 247, no. 4940, p. 286–293.

Wald, D.J., Burdick, L.J., and Somerville, P.G., 1988, Simulation of acceleration time histories close to large earthquakes, *in* Von Thun, J.L., ed., Proceedings; Earthquake Engineering and Soil Dynamics II; recent advances in ground-motion evaluation: American Society of Civil Engineers Geotechnical Special Publication 20, p. 430–444.

Wald, D.J., Helmberger, D.V., and Hartzell, S.H., 1990, Rupture process of the 1987 Superstitions Hills earthquake from the inversion of strong-motion data: Seismological Society of America Bulletin, v. 80, no. 5, p. 1079–1098.

Wald, D.J., Helmberger, D.V., and Heaton, T.H., 1991, The rupture initiation process of a large earthquake; Loma Prieta [abs.]: Seismological Research Letters, v. 62, no. 1, p. 29.

Wald, D.J., Somerville, P.G., and Helmberger, D.V., 1987, Compatibility of accelerograms of the 1979 Imperial Valley earthquake with slip-distribution asperity models [abs.]: Seismological Research Letters, v. 58, no. 1, p. 10.

Wallace, T.C., Velasco, A.A., Zhang, Jiajun, and Lay, Thorne, 1991, A broadband seismological investigation of the Loma Prieta, California, earthquake; evidence for deep slow slip?: Seismological Society of America Bulletin, v. 81, no. 5, p. 1622–1646.

Working Group on California Earthquake Probabilities, 1988, Probabilities of large earthquakes occurring in California on the San Andreas Fault: U.S. Geological Survey Open-File Report 88–398, 62 p.